T.R.
BOLU ABANT İZZET BAYSAL UNIVERSITY
INSTITUTE OF GRADUATE STUDIES
Department of Physics

FABRICATION OF Al/Gd_2O_3/P-Si/Al DIODES AND EVALUATION OF ELECTRICAL PARAMETERS UNDER IRRADIATION

MASTER OF SCIENCE

HUSAM RAED SABEEH AL-ESAİFER

ACADEMIC SUPERVISOR
Assoc. Prof. Dr. Aliekber AKTAĞ

ACADEMIC CO-SUPERVISOR
Prof. Dr. Uday Muhsin NAYEF

BOLU, MAYIS - 2022

APPROVAL OF THE THESIS

Fabrication of Al/Gd_2O_3/p-Si/Al diodes and evaluation of electrical parameters under irradiation submitted by **Husam Raed Sabeeh Al-Esaifer** and defended before the Examining Committe Members listed below in partial fulfillment of the requirements for the degree of **Master of Science** in **Department of Physics, Institute of Graduate Studies of Bolu Abant İzzet Baysal University in 12.05.2022.**

Examining Committee Members	**Signature**
Supervisor Assoc. Prof. Dr. Aliekber AKTAĞ Bolu Abant Izzet Baysal University	....
Member Assoc. Prof. Dr. Erhan BUDAK Bolu Abant Izzet Baysal University	....
Member Assoc. Prof. Dr. Ayşegül KAHRAMAN Bursa Uludağ University	....

Prof. Dr. İbrahim KÜRTÜL
Director of Institute of Graduate Studies

ETHICAL DECLARATION

In this thesis dissertation that was properly prepared according to the Thesis Writing Rules of Bolu Abant İzzet Baysal University of the Institute of Graduates Studies, I hereby declare that;

- All data, information, and documents presented in the thesis were obtained in accordance with the academic and ethical rules,
- All data, documents, assessments, and results were presented in accordance with the scientific ethical and moral rules,
- All works that were benefitted in the thesis were appropriately cited,
- No alteration was made in the data used,
- Study presented in this thesis is original,

Otherwise, I declare that I accept the loss of all my rights in case any contradiction that may arise against me.

Based on the plagiarism report that was generated on the date of 11/04/2022 by using predetermined filtrations set by Directorate of Institute of Graduate Studies of the Turnitin programme, a plagiarism detection sofware, the rate of plagiarism detected was 16 %.

____

HUSAM RAED SABEEH AL-ESAIFER

ABSTRACT

FABRICATION OF Al/Gd_2O_3/P-Si/Al DIODES AND EVALUATION OF ELECTRICAL PARAMETERS UNDER IRRADIATION
MSC THESIS
HUSAM RAED SABEEH AL-ESAİFER
BOLU ABANT İZZET BAYSAL UNIVERSITY
INSTITUTE OF GRADUATE STUDIES
DEPARTMENT OF PHYSICS
(SUPERVISOR: ASSOC. PROF. DR. ALİEKBER AKTAĞ)
(CO-SUPERVISOR: PROF. DR. UDAY MUHSİN NAYEF)
BOLU, MAY 2022
(XV + 50)

The present study focused on the crystal structure, morphology, dielectric and electrical properties of n-type gadolinium oxide (Gd_2O_3) on p-type Czochralski-grown monocrystalline (CZ) silicon (100) wafers (CZ-pSi) as well as on glass, and determination of gamma rays' effects on Gd_2O_3/(CZ-pSi) diodes. The growth of the Gd_2O_3 layers was carried out by pulsed laser deposition technique (PLD) using altered laser energies (500, 600, 700, 800 and 900 mJ). Several Gd_2O_3/(CZ-pSi) diode samples were fabricated at room temperature and pressure (3.3 x10^{-2} Pa). The front and rear Al metal contacts were added to finalize Al/Gd_2O_3/(CZ-pSi)/Al devices. The surface morphology of the Gd_2O_3 layers was determined by AFM imagining. Surface roughness root mean square (RMS) calculations revealed that spherical shaped particles ~20-30 nm in diameter are present on the surface. The pulse laser energy has enormous effect on the grow of Gd_2O_3 layers, their particle sizes, deposition rates and surface morphology. Therefore, the membrane thickness decreases with increasing applied laser power to the target formed on the silicon wafer. UV-Vis studies displayed that the band structure for Gd_2O_3 layers on glass with substantial absorption at 290 nm has been formed the largest bandgap 3.46 eV for Gd_2O_3 film deposited at 800 mJ laser energy. Current-Voltage (I-V) measurements of the as-synthesized Al/Gd_2O_3/(CZ-pSi)/Al diodes were carried out for different laser power before irradiation. Other than a tiny increase in the semi-logarithmic representation at the beginning of the curves all curves indicate similar and typical leakage current behavior through oxides. All curves have a steeper rise above a certain voltage

suggesting a change in the predominant charge transport mechanism. The capacitance-voltage (C-V) measurements of Gd_2O_3 films with different laser energies show similar behavior in frequency-dependent measurements. The capacitance values of Al/Gd_2O_3/(CZ-pSi)/Al diodes declined until -3V (totally depleted voltage). According to the findings the junction capacitance is inversely proportional to the reverse biased and directly proportional to the active voltages of Al/Gd_2O_3/(CZ-pSi)/Al diodes. Electrical property changes were evaluated under the influence of gamma ray radiation doses (3, 6, 12, 18, 24, 30, 36, 42 and 50 Gy) using Co-60 as the gamma ray source for Gd_2O_3/(CZ-pSi) deposited in 500 mJ laser energy at the frequency of 100 kHz. In the I-V curves, it was revealed that the current started to decrease with increasing radiation doses and continued to decrease in the direction of approaching zero with increasing radiation doses. In C-V curves, it turned out that there is a continuous shift in curves to the right of the pre-radiation curves which remains and increases with increase of radiation doses. The magnitudes of oxides capacitance shift up as the doses varies from 0 to 50 Gy. A specific sensitivity value was determined to be 44.8 ± 2.9 mV/Gy for 50 Gy dose.

KEYWORDS: Semiconductors, Pulsed Laser Deposition, Gadolinium Oxide, High k-dielectric oxides, Radiation, Gamma rays.

ÖZET

Al/Gd_2O_3/P-Si/Al DİYOTLARININ ÜRETİMİ VE IŞINLAMA ALTINDA ELEKTRİKSEL PARAMETRELERİNİN DEĞERLENDİRİLMESİ
YÜKSEK LİSANS TEZİ
HUSAM RAED SABEEH AL-ESAIFER
BOLU ABANT İZZET BAYSAL ÜNİVERSİTESİ
LİSANS ÜSTÜ EĞİTİM ENSTİTÜSÜ
FİZİK ANABİLİM DALI
(TEZ DANI ŞMANI: DOÇ. DR. ALİEKBER AKTAĞ)
(İKİNCİ DANIŞMAN: PROF. DR. UDAY MUHSİN NAYEF)
BOLU, MAYIS - 2022
(XV + 50)

Bu çalışma n-tipi gadolinyum oksitin (Gd_2O_3), p-tipi Czochralski tarafından büyütülen monokristal (CZ) silikon (100) alttaşlar (CZ-pSi) ve cam üzerine büyütülmüş filmlerin yapısı, morfolojisi, dielektrik ve elektriksel özelliklerine ve ayrıca gama ışınlarının Gd_2O_3/(CZ-pSi) diyotları üzerindeki etkilerinin belirlenmesine odaklanmıştır. Gd_2O_3 katmanlarının büyümesi, farklı lazer enerjileri (500, 600, 700, 800 ve 900 mJ) kullanılarak atımlı lazer film büyütme tekniği (PLD) ile gerçekleştirildi. Birkaç Gd_2O_3/(CZ-pSi) diyot örneği, oda sıcaklığında ve $3.3x10^{-2}$ Pa basınç altında üretildi. Son olarak, Al/Gd_2O_3/(CZ-pSi)/Al cihazlarını tamamlamak için ön ve arka Al metal kontaklar eklendi. Gd_2O_3 katmanlarının yüzey morfolojisi, AFM görüntülemesi ile belirlendi. Yüzey pürüzlülüğü ortalama kare (RMS) hesaplamaları, yüzeyde ~20-30 nm çapında küresel şekilli parçacıkların bulunduğunu ortaya koydu. Atımlı lazer enerjisinin Gd_2O_3 katmanlarının büyümesi, parçacık boyutları, biriktirme oranları ve yüzey morfolojisi üzerinde muazzam bir etkisi bulunmaktadır. Bu nedenle silikon alttaş üzerinde oluşturulan hedefe uygulanan lazer gücü arttıkça film kalınlığı azalmaktadır. UV-Vis çalışmaları, 290 nm'de önemli ölçüde soğurmaya sahip cam üzerindeki Gd_2O_3 katmanları için bant yapısının, 800 mJ lazer enerjisinde biriktirilen Gd_2O_3 filmi için en büyük bant aralığı 3.46 eV'yi oluşturduğunu göstermiştir. Üretilen Al/Gd_2O_3/(CZ-pSi)/Al diyotların gama ışınlaması öncesi farklı lazer güçleri için Akım-Gerilim (I-V) ölçümleri yapılmıştır. Eğrilerin başlangıcındaki yarı logaritmik grafiklerindeki küçük artışlar dışında, tüm eğriler benzer tipik kaçak akım davranışı göstermiştir. Tüm eğriler, baskın yük taşıma mekanizmasında bir değişiklik olduğunu düşündüren belirli bir voltajın üzerinde daha dik bir artışa sahiptir. Farklı lazer enerjileriyle büyütülmüş Gd_2O_3 filmlerinin Kapasitans-Voltaj (C-V) ölçümleri, frekansa bağlı ölçümlerde de benzer davranış göstermektedir. Al/Gd_2O_3/(CZ-pSi)/Al diyotların kapasitans değerleri -3 V'a (gerilim sıfıra düşene) kadar düşmüştür. Elde edilen bulgulara göre kapasitans Al/Gd_2O_3/(CZ-pSi)/Al diyotların ters kutupluluğu ile ters orantılı ve aktif gerilimleri ile doğru orantılıdır. Elektriksel özellik değişiklikleri, Gd_2O_3/(CZ-pSi) için gama ışını kaynağı olarak Co-60 kullanılarak gama ışını radyasyon dozlarının (3, 6, 12, 18, 24, 30, 36, 42 ve 50 Gy) etkisi 100 kHz frekansında 500 mJ lazer enerjisinde üretilen filmler ile değerlendirildi. I-V eğrilerinde, artan radyasyon dozları ile akımın azalmaya başladığı ve artan radyasyon dozları ile sıfıra yaklaşma yönünde azalmaya devam ettiği ortaya çıktı. C-V eğrilerinde ise, radyasyon öncesi eğrilerin sağında kalan ve radyasyon dozlarının artmasıyla artan eğrilerde sürekli bir kayma olduğu ortaya çıktı. Dozlar 0 ile 50 Gy arasında değiştikçe oksit kapasitansının değerleri arttı. 50 Gy doz için özel duyarlılık değeri 44,8 ± 2,9 mV/Gy olarak belirlendi.

ANAHTAR KELİMELER: Yarıiletkenler, Atımlı lazer film büyütme, Gadolinyum oksit, Yüksek k-dielektrik oksitler, Radyasyon, Gama ışınları.

TABLE OF CONTENTS

Page

LIST OF FIGURES

Page

LIST OF TABLES

Page

LIST OF PICTURES

Page

LIST OF ABBREVIATIONS AND SYMBOLS

φ_{ms}	: Work function difference between metal and semiconductor
A	: constant
a	: Lattice Constant
AFM	: Atomic Force Microscopy
CMOS	: Complementary Metal Oxide Semiconductor
Co-60	: cobalt-60
C-V	: Capacitance - Voltage Characteristic
d	: Film thickness
d_{hkl}	: Lattice Spacing
E_g	: Optical band gap
F.C.C	: Face-Centered Cubic
FTIR	: Fourier-Transform Infrared Spectroscopy
Gd_2O_3	: Gadolinium Oxide
h, k, l	: Miller Indices
I-V	: Current-Voltage Characteristic
MOS	: Metal-Oxide-Semiconductor
MOSFET	: Metal Oxide Semiconductor Field Effect Transistor
PLD	: Pulsed Laser Deposition
Q_b	: Depletion charge
Q_i	: Inversion charge
$q_{\phi s}$	: Energy difference between vacuum levels E_{vac} and Fermi level E_F
RCA	: Radio Corporation of America
RMS	: Root Mean Square
SEM	: Scanning Electron Microscopy
T	: Specific transmittance in the wavelength range
UV-Vis	: Ultraviolet –visible spectroscopy
V_{fb}	: Flat-band Voltage
x_a	: Space charge zone
XRD	: X-Ray Diffraction analysis
α	: Absorption coefficient
λ	: Wavelength

ACKNOWLEDGEMENTS

I would like to express my deepest gratitude to my supervisor Assoc. Dr. ALİEKBER AKTAĞ and co-supervisor Prof. Dr. UDAY MUHSİN NAYEF for their guidance, advice and all the scientific and moral support they provided during the research period.

I would also like to thank Prof. Dr. ERCAN YILMAZ for his scientific guidance.

I also thank the technical assistance of Mr. EMRE DOĞANCI with gratitude.

Finally, I offer this humble effort to my mother's soul. I also extend my thanks and gratitude to my family, especially my wife SURA AL-QAZZAZ, my friends, and everyone who gave me moral support and encouragement.

I also thank to the Bolu Abant Izzet Baysal University, Nuclear Radiation Detectors Application and Research Center (NÜRDAM), Turkey, the University of Baghdad, and University of Technology, Department of Applied Sciences, Iraq for allowing me to use their facilities.

This study was supported by the Presidency of Turkey, Presidency of Strategy and Budget under Contract Number: 2016K12-2834.

1. INTRODUCTION

During the last few decades, significant technical progress has been achieved in the production of various nanostructures through different material combinations for micro- and nanoelectronics. To meet the need for ever higher power densities, ever more precise methods are required to satisfy the requirement for producing such structures. The development of, among other things, molecular beam epitaxy has paved the way for production, and simplification contributed to the production of modified layer structures and nanostructures for transistors. Due to the progressive scaling of such components, for example, the layer thickness of the gate dielectric (SiO_2) in the metal oxide semiconductor, the field-effect transistors (MOSFET) are getting thinner. This is creating quantum effects such as the tunneling effect, which play an increasingly important role [1, 2].

At a layer thickness of SiO_2 of 1.5 nm, the leakage current is already in the range of 10 A/cm^2, which is considered a limit for the functionality of such a layer device [3]. A loss of the insulation properties of the gate dielectric causes device failure, which is why others substitute materials have to be found. By modifying the crystalline structure of such materials, further enhanced properties can be adjusted and improved. Furthermore, the geometry and the general structure of such a component can be fundamentally changed by integrating nanostructures. When looking at complementary metal-oxide-semiconductor (CMOS) technology, gate capacitance C plays a decisive role and should not be reduced in the new technology generation. The layers must have a higher thickness, so that the leakage current through them can be reduced. However, to the capacity not to be reduced, these materials must exhibit an increased dielectric constant. Such materials are also called high-k materials.

1.1 High-k Dielectric Materials

In addition to the increased dielectric constant, high-k materials have to meet a wide variety of requirements in order to provide functionality in the component. First of all, there must be sufficient insulation properties due to a large band gap and symmetrical band arrangement presented in silicon. Furthermore, thermodynamic and chemical stability in contact with silicon and the other materials that are in direct contact with the components. The interface quality and surface morphology also play an important role. In addition, the compatibility with technological manufacturing processes of different components must be accompanied by the compatibility with chemical solvents and with wet and dry etching processes.

The first variants used were silicon nitride (Si_3N_4) and silicon oxynitride (SiO_xN_y), where only a slight increase in dielectric constant can be reached to approximately $\varepsilon_r \approx 7$ [4, 5]. Later on, many different materials with higher dielectric constants were being investigated as Substitutes for SiO_2, e.g. B. HfO_2, Al_2O_3, ZrO_2, TiO_2, and Ta_2O_5 [6-10]. Unfortunately, some of these materials are not thermodynamically stable in contact with silicon and are therefore not suitable as replacement for SiO_2 [11]. As a promising material, particularly Hafnium Oxide (HfO_2) has been demonstrated to work even in Intel's 45 nm technology [12]. In addition to the high dielectric constant, it is distinguished by the simple manufacturing process and the chemical and thermodynamic stability in contact with silicon. HfO_2 exhibits these properties in the amorphous structure, eliminating the disadvantage of the crystallization of the layer in high-temperature processes is what can lead to an increase in leakage current [13].

In addition, many high-k materials show the formation of an amorphous intermediate layer during growth or deposition on silicon, consisting of SiO_2 or a combination of Si and the High-k material [13]. An amorphous intermediate layer with a lower dielectric constant can significantly reduce the total capacitance. In addition, the band gap decreases with increasing dielectric strength constant, as a result of which the leakage current can increase [14]. Furthermore, the compatibility with the established technological processes for the production of MOSFET structures plays a decisive role. For high-k materials, metals must be used as contact material, for this purpose the coating and etching methods are needed to become incorporated into the process. Also, many materials can come into contact with chemical solvents. Therefore, suitable protection is needed. Another disadvantage of high-k materials is the reduction in charge carrier mobility in the vicinity of the interface with silicon, due to the scattering of charge carriers at interface states and lattice vibrations [15-17]. In contrast, it is possible through a targeted modification of the structure to influence the interface [18].

1.2 Rare Earth Oxides

The gadolinium oxide (Gd_2O_3) examined in this work is one of the rare earth oxides, which have become more and more important in the last few decades due to its use in various applications [19]. In addition to being used as a catalyst in the automotive industry as a substitute for precious metals, rare earth oxides are also utilized as an addition in the glass industry to increase the quality of the optical characteristics and chemical stability [20, 21]. Rare earth oxides are also utilized in ceramics to create hydrophobic surfaces and as a battery, additive to increase performance [22, 23]. In microelectronics, the rare earth oxide is investigated to be used as a high-k dielectric in MOSFET structures [24-26]. Some of the rare earth oxides have high dielectric constants and are chemically and thermodynamically stable in contact with silicon [11].

Most high-k materials are used in their amorphous structure. The rare earth oxides, however, can also be used in their crystalline form. Because they have sufficient insulating properties, which enables the possibility of manufacture by epitaxial growth. For growth epitaxial layers must be a for the layer and substrate material there is some agreement in symmetry and lattice constants.

Most rare earth oxides occur exclusively in the stoichiometry Ln_2O_3 and most often form three different polymorphs crystal structures from the cubic C-type in the bixbyite structure, the monoclinic B-type, and the hexagonal A-type [27, 28].

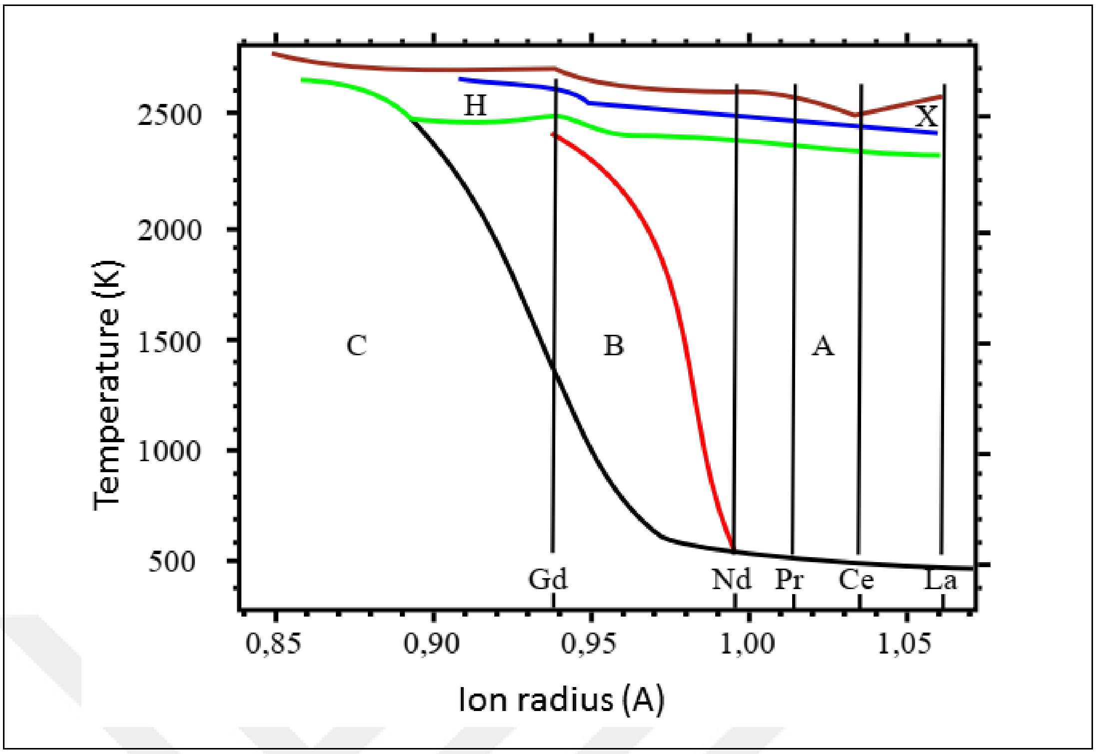

Figure 1.1. Phase diagram of the rare earth oxides, where the ion radius is plotted as a function of the temperature.

The different phases are with the Letters C for cubic, B for monoclinic, and A for marked hexagonally. The H and X phases are special high-temperature phases. According to [27, 28, 29].

The predominant structure depends on the temperature, the hydrostatic pressure and the ionic radius of the rare-earth ion [27]. Figure 1.1 shows the relationship between crystal structure and temperature for the different rare earth oxides. The crystal structure has a decisive influence on the dielectric characteristics [30]. For the rare earth oxides with the ions La3+ to Nd3+ is the hexagonal A-type structure and for rare earth oxides with ions of a higher atomic number the cubic C-type structure is the most common. For the growth on Si (001), the cubic C-type structure has the smallest lattice mismatch and will so preferably evaluate. The C-type structure can be represented by the unit cell of the mineral bixbyite, which can be described using calcium fluorite (CaF_2) [31]. The bixbyite structure has the space group Ia3 and contains 32 metal atoms and 48 oxygen atoms per unit cell, one-fourth of the oxygen atoms are vacant along with the space diagonal and the metal atoms are six-coordinate [27, 28].

In recent years, some rare earth oxides have been investigated for MOS applications. Including praseodymium oxide (Pr_2O_3), it has been grown epitaxially on Si (001) and extensively characterized with different methods [32]. For praseodymium oxide, however, many stable stoichiometries are known, which can convert into one another even with small differences in the growth or process conditions [33], and thus the electrical properties can vary greatly.

Cerium oxide (CeO_2) was also used as a high-K material examined. However, it can also relatively simply take/release oxygen atoms reducing conditions, whereby different stoichiometries can develop, which makes handling it rather difficult [34]. Furthermore, became many other materials like Er_2O_3 [35], Sm_2O_3 [36], and Nd_2O_3 [37] have been investigated, none of which was able to establish itself for use in MOS structures.

1.3 Gadolinium Oxide (Gd_2O_3)

In this work, the material gadolinium oxide was used, which is one of the most promising candidates for use as a high-k material. Gd_2O_3 has a large band gap, asymmetrical one band arrangement to silicon, low leakage currents, good interface properties, and a high dielectric constant [38]. Gd_2O_3 also has the smallest lattice mismatch of the rare earth oxides compared to silicon and is thermodynamically stable in contact with Silicon, which enables epitaxial growth.

There are three different crystal phases for the rare-earth oxides Gd_2O_3: they are the cubic C-type, the hexagonal A-type, and the monoclinic B-type [27]. Only the cubic structure was seen for bulk material and standard circumstances. The crystal structure can change to a monoclinic or hexagonal structure at high temperatures and pressures [27][39]. The phase diagram in Figure 1.1 shows the transition from cubic to the monoclinic phase of Gd_2O_3 at ~ 1300 K to hexagonal phase at ~ 2400 K.

For the growth on silicon possesses the cubic phase of Gd_2O_3 has a suitable symmetry. With the lattice constant of cubic Gd_2O_3 (a = 1.0811 nm [40]) the lattice mismatch results in relation to double the lattice constant of silicon ($2a$ = 1.0862 nm [41]) is about 0.5%.

In principle, the epitaxy of Gd_2O_3 should therefore have the same orientation to the substrate. However, the surface energies are also the different orientations an important factor for the crystal orientation. The surface energy of the (100) orientation is somehow larger than those with the (110) and (111) orientations [42].

XPS studies have shown that Gd_2O_3 binds to silicon via oxygen, i.e. Gd-O-Si bonds predominate at the interface [38]. Gd_2O_3 grows on Si (111) in the same (111) orientation [43].

For the growth on Si (001), however, Gd_2O_3 forms a (110) orientation from what a close match of the oxygen sublattice in this direction and the lower surface energy can be justified [38],[44]. There are also reports in the growth of Gd_2O_3 on Si (001) at low temperatures or on a surface with altered surface reconstruction. This orientation is due to the alternating arrangement of the positive and negative ions of a two-dimensional electron gas (2DEG) conceivable formation, which for electronic applications would be interesting [45-47]. Furthermore, in the literature, the occurrence is also non-cubic phases in thin Gd_2O_3 films when growing on different substrates and under different growth conditions.

When Gd_2O_3 is grown over GaN, SiC, or GaAs, the crystal structure changes from hexagonal to monoclinic as the layer thickness increases [48-50]. The monoclinic structure is formed by the growth of Gd_2O_3 on Si (111) at low temperatures [51]. A combination of the cubic and monoclinic phases of Gd_2O_3 was discovered on Ge (001) [52]. Depending on the temperature or chemical potential of oxygen discovered, the monoclinic phase emerges in various growth studies, such as sputtering or laser molecular beam epitaxy of Gd_2O_3 on Si (001) [53, 54]. Overall, systematic studies on the general conditions for the stabilization of certain polymorphs in thin layers are hardly available. Furthermore, a general knowledge of the physical mechanisms behind the creation of distinct phases in thin layers is currently lacking. The same situation is found for the characterization of the electrical and dielectric properties of Gd_2O_3 layers with different crystal structures.

1.4 PN Junction Diode

The PN diode is one of the most important electronic devices. PN device is obtained by combining two types of semiconductors, the excessive negative (N-type) and the excessive positive (P-type) electric charge semiconductors. Well known that two types of diodes are produced from silicon, and germanium. Most of the resistance of the PN junction is concentrated in the *depletion* layer that has no excess charge of any type and its resistance is relatively large compared to the rest of the semiconductor P and N regions. The presence of opposite two charges separated by a distance will create an electric field, which in turn leads to the creation of electric potential. As a result of the transfer of charge carriers between the two halves of the junction, the number of electrons in the P-type layer increases, and the number of holes in the N-type layer also increases, thus forming between the two regions, generating an electric field opposite to the movement of the charge carriers. The equilibrium occurs, as the free electrons are not able to cross from N to P type due to the opposite force resulting from the generated field, and similarly the holes in P are not be able to cross into N region for the same reason. In equilibrium, the inlet electric field leads a generation of a potential barrier. The generated barrier voltage is called the junction voltage (V_B). Its value depends on the material type. For example, the junction voltage for silicon is $V_B = 0.7$ V, and for germanium, $V_B = 0.3$ V. Figure 1.2 shows the connection of the PN diode with the barrier voltage.

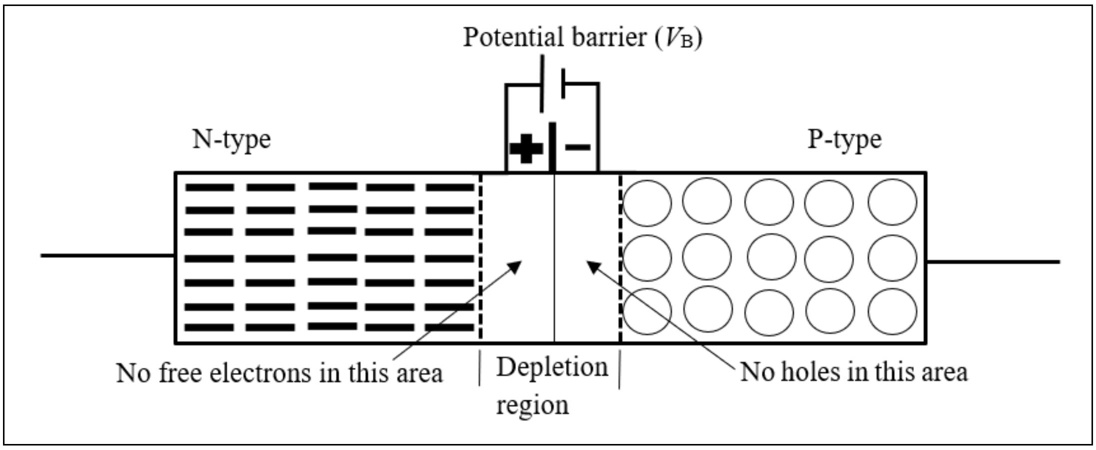

Figure 1.2. Barrier voltage (V_B) in a PN diode.

The diffusion of electrons and holes across the PN junction not only results in the depletion layer but also changes the energy levels through junction. It is observed in Figure 1.3.(a) that the energy bands before the electrons diffuse through the junction. The P-type side contains many holes in the valence band, while the N-type side contains many free electrons in the conduction band. It is also noted that the energy bands of the P-type layer have been plotted a little higher than the energy bands of the N-type layer. The reason for this is that the bonding of electrons to the nucleus of pentavalent atoms is stronger than the bonding of electrons to the nucleus of trivalent atoms, and therefore the potential energy of electrons in pentavalent atoms is smaller than the potential energy of electrons in triple valence atoms, meaning that the energy needed to liberate them is larger. Therefore, the orbitals of a trivalent atom P-type side are slightly larger than the orbitals of a pentavalent atom N-type side and this explains why the P bands are slightly higher than the N bands. Figure 1.3.(b) The energy diagram after the equilibrium is achieved and it is noted that the P-type have moved upwards relative to the N-type due to the electron crossing the junction, it will fill the gap of one of the trivalent atoms and thus this extra electron will raise the orbit of the conduction band away from the triple atom, or in other words that any other electron that comes to the P-type layer will need more energy than the energy of the previous electron to enter the orbit of the conduction band, and this is the reason for the movement of P-type bundles to the top relative to N-type bundles after that A layer of depletion has been formed [55].

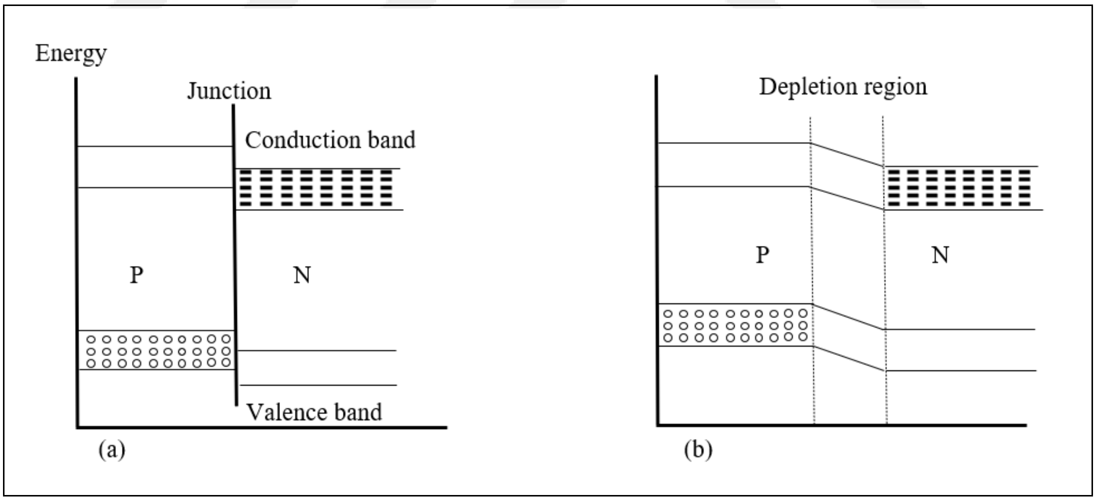

Figure 1.3. PN junction energy diagram.

1.5 Material Characteristics Modifications Under Gamma Rays

A worldwide initiative to replace SiO_2 with high-k dielectrics has been spurred by the urgent need to lower gate leakage current in nanoscale metal-oxide-semiconductor (MOS) devices. Since the beginning of high-k technology, the dependability of high-k dielectrics has been a source of great interest. Numerous theoretical and experimental research has been conducted on the crystal structure and electrical characteristics of metal oxide thin films.

High-energy radiations, such as gamma rays, alter the physical characteristics of the materials they permeate, and these changes are highly reliant on the structure of the substances absorbed. It is believed that exposure to ionizing radiation (Gamma-ray) produces structural problems (called color centers or oxygen vacancies in oxides). The effect of radiation is dependent on both the film properties, such as thickness and dose. The deterioration is more severe for thinner films with greater doses. Radiation absorption in thin films is determined by their electronic structure, which is altered by photon interaction.

The capacity to synthesize high-energy source particles, which allows for the formation of high-quality film at natural substrate temperatures, is the major benefit of pulsed laser deposition (PLD). As a result, the purpose of this study is to evaluate the effect of irradiation using a Co-60 gamma-ray source on Gd_2O_3/(CZ-pSi) diodes and to measure its electrical properties grown via PLD.

2. AIM AND SCOPE OF THE STUDY

This study aims to evaluate electrical parameters of Al/Gd_2O_3/(CZ-pSi)/Al diodes under irradiation and study the effect of growth parameters on structure, morphology, dielectric, electrical properties, and also optical properties of Gd_2O_3 films deposited on glass.

In fabrication process, the Gd_2O_3 layers were grown by the Pulsed Laser Deposition (PLD) technology with different building energies and the resulting thicknesses were calculated for each energy.

To identify parameters, measurements of current-voltage (I-V) and capacitance voltage (C-V) characteristics before and after irradiation at 3-50 Gy dose range were performed by Co-60 gamma source.

3. MATERIALS AND METHODS

In this chapter measurement methods used in epitaxially growth of Gd_2O_3 layers are presented.

The Gd_2O_3 target was purchased from Ganzhou Wanfeng Adv. Materials Tech. Co., Ltd. 99.99% pure Gd_2O_3 was used without any further purifications. Full details of sample specifications are given in Appendix 1.

Several Al/Gd_2O_3/(CZ-pSi)/Al diode samples were fabricated. n-type Gd_2O_3 layers were deposited on CZ p-type silicon (100) wafers and on glass substrates at varied laser energies (500, 600, 700, 800 and 900 mJ) by the Pulse Laser Deposition (PLD) technique at room temperature and pressure (3.3 x 10^{-2} Pa). Lastly rear and front metal contacts were added to form final device.

Gd_2O_3 samples were characterized by X-ray diffraction (XRD), scanning electron microscopy (SEM), atomic force microscopy (AFM), and Fourier transform infrared spectroscopy (FTIR).

Co-60 gamma source was used to irradiate the samples at a dose rate (3, 6, 12, 18, 24, 30, 36, 42, and 50 Gy).

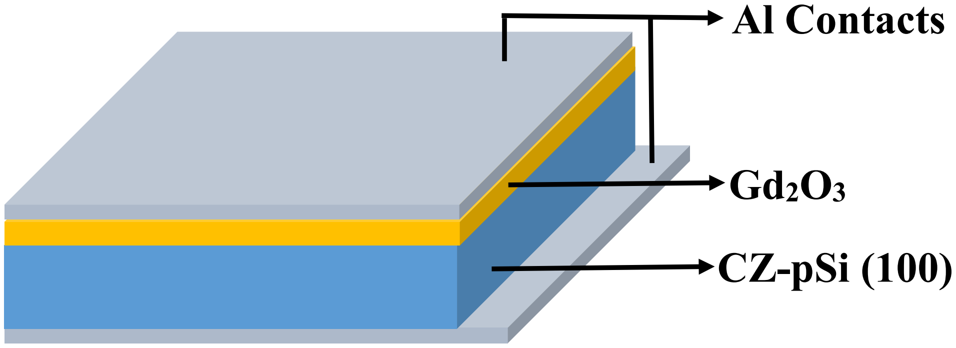

Figure 3.1. Gd_2O_3/(CZ-pSi) diode components.

3.1 X-Ray Diffraction (XRD) and Crystal Structure Analysis

The first discovery and explanation of diffraction effects was provided by W. L. Bragg [54] when a crystalline material was examined by X-rays.

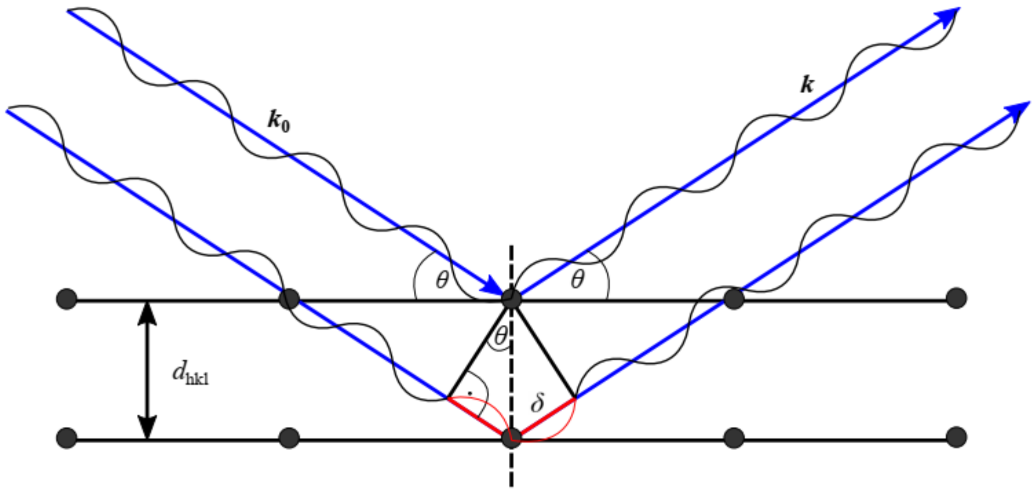

Figure 3.2. Schematic representation of the Bragg condition for the diffraction of X-rays on a crystal with the lattice plane spacing d_{hkl} at the angle of incidence θ.

A set of lattice planes of a crystal parallel to the surface with the distance d_{hkl} labelled with the miller indices (*hkl*) is considered. When X-rays of the wavelength λ hit the crystal lattice points they are reflected. According to the law of reflection, the angle of incidence and the angle of reflection are equal. Due to the very small wavelength of the X-rays, it can penetrate into the crystal and also to the underlying network levels and reflect back. Overall, a longer pathway back than the rays reflected on the surface, whereby these two rays or waves are out of phase. The difference in the distance covered is referred to as the path difference 2δ. When emerging from the surface, these rays can interfere with the rays reflected on the surface, whereby a constructive interference occurs with a path difference of the magnitude of integer multiples of the wavelength, as is illustrated in Figure 3.2.

The condition for constructive interference is therefore determined through the angle of incidence θ between the incident ray and the plane of the mesh. The angle θ depends on the lattice plane spacing d_{hkl} and the wavelength λ of the incident X-ray radiation. The context is described by the Bragg equation (1) where *n* indicates the diffraction order. The equation (1) also applies to the path difference: $2\delta = n\lambda$ with $d_{hkl} = \delta / \sin\theta$.

$$n\lambda = 2d_{hkl} \sin\theta \quad (1)$$

The lattice constant *a* can be determined with the knowledge of the crystal structure. Equations (2) and (3) describe the relationship between lattice plane spacing and the lattice constant of the cubic and monoclinic crystal structure. The variables *a*, *b* and *c* are the different lattice constants, and *h*, *k*, and *l* are the Miller indices, which are used to describe the lattice planes.

$$d_{hkl} = \frac{a}{\sqrt{h^2+k^2+l^2}} \quad (2)$$

$$d_{hkl} = \frac{1}{\sqrt{\frac{h^2}{a^2 sin^2\beta}+\frac{k^2}{b^2}+\frac{l^2}{c^2 sin^2\beta}-\frac{2hl cos\,\beta}{ac sin^2\beta}}} \quad (3)$$

All lattice planes and lattice directions are described by Miller parameters (*hkl*), which is a mathematical description by which we can learn specifications and discussions about planes and special crystal directions of surfaces or within masses in the crystal of the bulk group's lattice monocrystals. The cubic system lattice cubic represents the directionality [*hkl*] in the vector perpendicular to the surface of the exact plane or the so-called facet.

The set of planes is denoted by {*hkl*}, the directivity of the crystal by the form [*hkl*], and the directivity of the group by the form of <*hkl*>. The directivity of Miller's coefficient in the simple cubic system is perpendicular to crystal planes. Figure 3.3 shows three general planes of Miller's modulus and they belong to the planes (111), (110), (100), respectively.

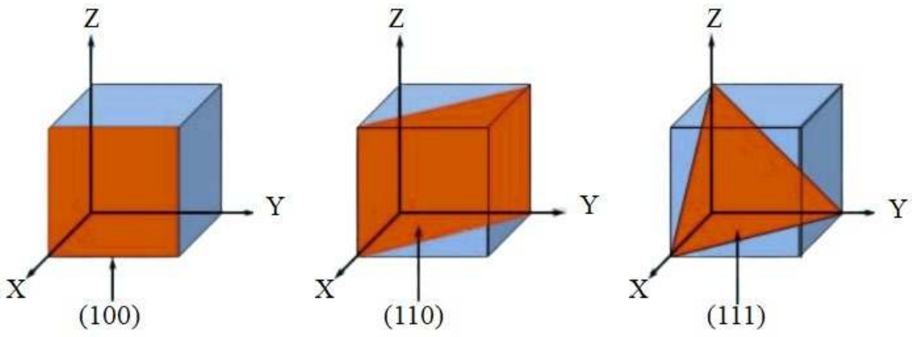

Figure 3.3. Miller indices of some planes in cube system (Daimon).

3.2 Scanning Electron Microscopy (SEM)

Before layer systems can be examined with the scanning electron microscope, the samples must be suitably prepared. The most important thing is to prepare the sample to the required thickness. However, the sample should be thick enough to contain enough information about the crystal structure. It also depends on which information obtained or which view of the layer system would like to be examined. In this work, the most frequently used views are plan views. For examination with the SEM, only a piece of the substrate in the top view is used. Furthermore, depending on the requirements for the examinations, attention must be paid to the orientation of the crystal during the preparation in order to be able to work with diffraction patterns of crystalline samples. All in all, the quality of the sample preparation is of great importance because this is decisive for the quality of the SEM images.

3.3 Atomic Force Microscopy (AFM)

Using atomic force microscopy (AFM) which has sufficient ability to produce clear microscopic images and good analysis of the sample surface and to characterize the surface topography of the precipitated Gd_2O_3 thin films and the effect of laser energies on them, we obtained through it several important information, including statistical values for the average grain size, distribution, average diameter, surface roughness, and root mean square (RMS).

3.4 Fourier Transform Infrared Spectroscopy (FTIR)

For FTIR measurements, infrared spectra of the deposition pattern were acquired at 15x magnification guided by reflection using a Bruker Vertex 70 FTIR Spectrometer Hyperion 3000.

3.5 Electrical Characterization

A capacitor structure that consists of a layer of metal, an oxide (e.g. SiO_2) and a semiconductor is known as a metal-oxide-semiconductor (MOS) capacitor. The semiconductor material is usually silicon. Metal is applied to contact the rear, which forms an ohmic contact. For the investigation of novel insulator materials, the MIS test structures are suitable for characterizing the dielectric properties of the layers with different electrical measurement methods. For understanding the physical processes in a MOS structure, first, the band structure in combination with p-doped silicon to be considered. The work function of the metal $q_{\phi m}$ or Semiconductor $q_{\phi s}$ is defined as the energy difference between vacuum levels E_{vac} and Fermi level E_F. The work function of the semiconductor is set together from the electron affinity of the semiconductor χ_s, the distance between the conduction band edge and the vacuum level, half the band gap $E_{g/2,}$ and the Fermi potential ϕ_F, which depends on the doping of the semiconductor [56]. The barrier height $q_{\phi B}$ that the charge carriers must overcome to get into the conduction band of the oxide results from the difference between the work function of the metal and the electron affinity of the oxide χ_{ox}. The ribbon tension is defined as the tension at which the ribbons run-flat, i.e. no stress drops across the oxide. In the ideal MOS capacitor, this results in flat band voltage V_{fb} from the exit potential difference of metal and semiconductor φ_{ms} (Eq. 4) [56].

$$V_{fb} = \varphi_{ms} = \varphi_m - \varphi_s = \varphi_m - (x_s + \frac{E_g}{2q} + \varphi_F) \quad (4)$$

When a voltage V_g is applied to the MOS capacitor, three different situations can occur. When creating a negative Voltage ($V_g < V_{fb}$) at the metal contact, majority charge carriers (here holes) from the semiconductor collect at the oxide/ Si interface, and the ligament is bent downwards. This situation of the MOS capacitor is called accumulation. The positive charge at the interface in silicon φ_s corresponds to the negative charge in the metal ($|\varphi_m| = \varphi_s$). If a positive voltage ($V_g > V_{fb}$) is applied, the ribbons bend upwards at the oxide / Si interface and the interface is depleted of majority charge carriers. This case is known as impoverishment. Forms at the interface, a depletion charge φ_b, which depends on the width of the space charge zone x_a and the doping of the silicon N_A ($\varphi_s = \varphi_b = -qN_Ax_a$). If the voltage increases further ($V_g >> V_{fb}$) there is an amplification of the band bending and more and more minority charge carriers (here electrons) collect at the interface. If the intrinsic energy level E_I at the oxide/Si interface is bent below the Fermi level, this condition is called inversion. The semiconductor charge then expands through the inversion charge φ_i and results in $\varphi_s = \varphi_b + \varphi_i$.

3.5.1 Current-Voltage Characteristic Measurements

We have used current-voltage (I-V) measurement to determine of electrical properties of the Al/Gd_2O_3/(CZ-pSi)/Al diode by a measuring device in dark conditions at room temperature.

Picture 3.1. I-V measurement system at NURDAM.

3.5.2 Capacitance-Voltage Characteristic Measurements

The Capacitance-Voltage (C-V) of the Al/Gd_2O_3/(CZ-pSi)/Al diode by a measuring device in dark conditions at room temperature. Voltage rating from -2 volts to 10 volts at frequencies 10, 20, 30, 40, 50, 60, 70, 80, 90, 100, 200, 300, 400, 500, 600, 700, 800, 900 and 1000 kHz. Then the capacitance values were obtained respectively for each voltage step at Origin Program.

Picture 3.2. C-V measurement system at NURDAM.

3.6 Gamma-ray Source

Co-60 chamber 900 was used as gamma rays' source at the dose rate of 0.0033 Gy/s. The effects of gamma rays on Al/Gd_2O_3/(CZ-pSi)/Al diode was studied at dose rates 3, 6, 12, 18, 24, 30, 36, 42 and 50 Gy at the frequency of 100 kHz.

Picture 3.3. Irradiator chamber 900 Co-60 gamma-ray source system at the University of Baghdad.

Table 3.1. Table showing the time period with the dose of gamma rays (Time/Dose).

Time/min	15	30	60	90	120	150	180	210	240
Dose/Gy	3	6	12	18	24	30	36	42	50

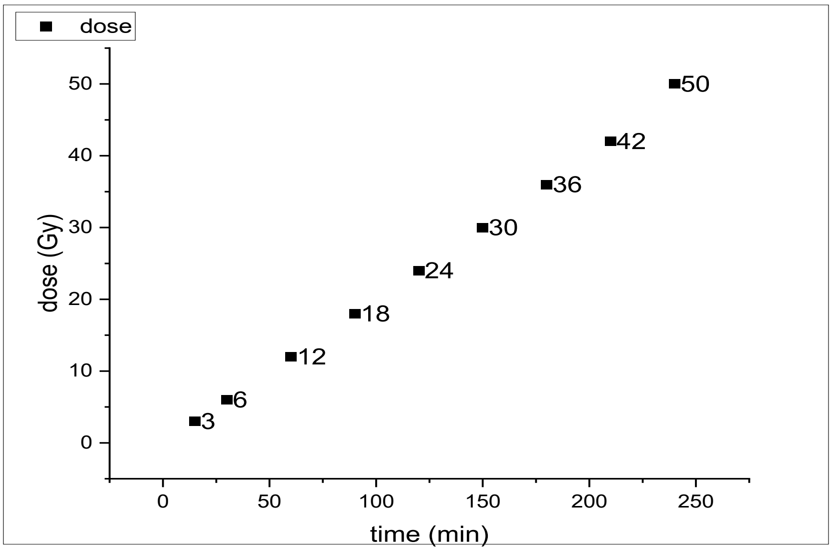

Figure 3.4. Gamma dose irradiations to films with time intervals.

3.7 Fabrication of Al/Gd_2O_3/(CZ-pSi)/Al Diode

The manufacturing process of Gd_2O_3/(CZ-pSi)/diode was carried out through the following three main stages:

3.7.1 Cleaning Process of Silicon Wafer

To remove contaminants that may be present on the surface of the silicon wafer the industry-standard RCA (Radio Corporation of America) procedure is adopted. To do it, the following steps are taken: Organic cleaning, oxide strip, and ionic cleaning.

a) Organic Cleaning: Organic cleaning removes organic pollutants using a 10:1:1 solution (distilled H_2O, H_2O_2, NH_4OH) heated to 60 °C, then the flakes are placed in the solution for 10 minutes and then placed in distilled water up to four dump cycles.

b) Oxide Strip: A solution of hydrofluoric acid (HF) with distilled water is prepared. The silicon wafers are then placed in a high-frequency solution for ten seconds. And then put it in distilled water for up to four dump cycles.

c) Ionic Cleaning: To remove ionic pollutants, such as Na+, Fe+ with 20 liters of deionized water, 2 liters of HCl, and 2 liters of H_2O_2 and then the silicon wafer is placed for ten minutes at 60 °C. After ten minutes the silicon wafers are placed in deionized water up to seven dump cycles.

3.7.2 Deposition Process by Pulsed Laser Deposition Technique (PLD)

Pulsed laser deposition (PLD) technology was used in the deposition process. On a p-type CZ (100) silicon-glass thin films (specifically “physical vapor deposition” PVD) at 200 pulses with energies 500, 600, 700, 800 and 900 mJ were considered by focusing the laser beam on the samples inside the vacuum chamber under pressure (3.3×10^{-2} Pa) at room temperature. The target consisting of a disk converted from powder to the solid-state of Gd_2O_3 evaporates in the plasma cloud then deposits as thin film on silicon wafer substrate.

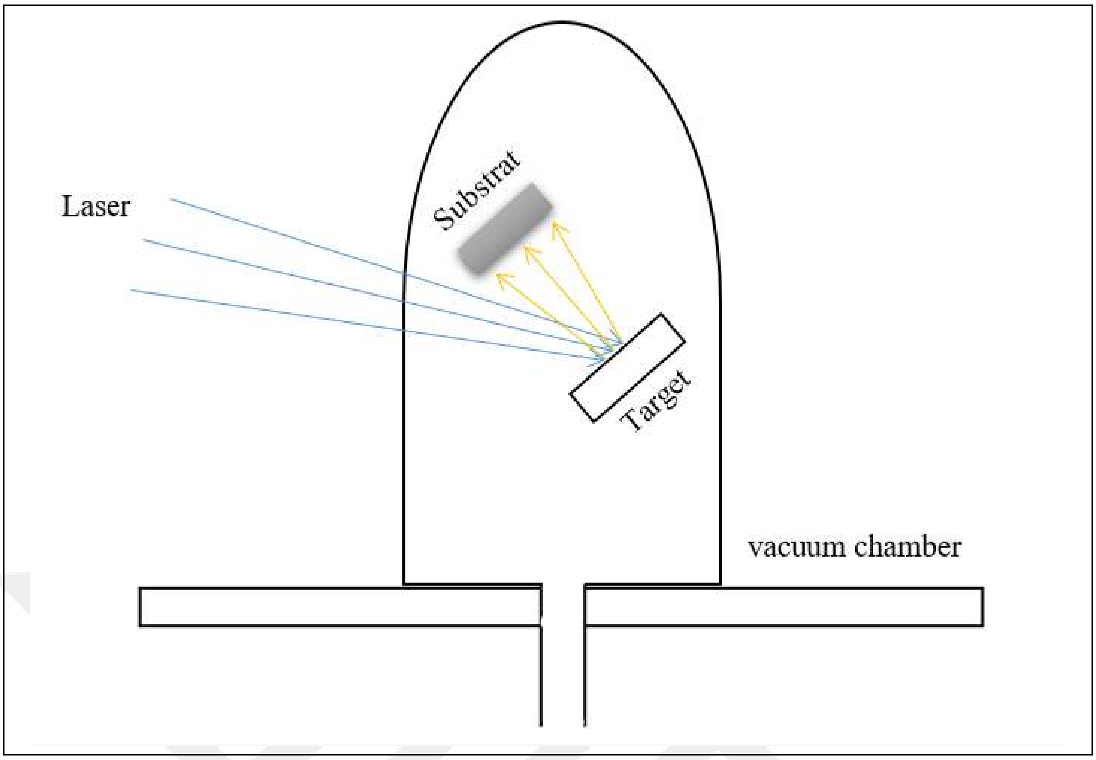

Figure 3.5. Illustration of a pulsed laser deposition (PLD) technique.

Picture 3.4. Deposition process by pulsed laser deposition technique (PLD) at the University of Baghdad.

3.7.3 Metal Contacts (Electrodes) Deposition

The contact electrodes for the prepared films are made by depositing 150 nm thick aluminum using a usual thermal evaporation method which is used to deposit metallic contacts on thin films by an Edward coating unit model (E610) under a high vacuum generated by a rotating and diffusion pump. In this procedure, the metal is put in a vacuum chamber with a pressure between 10^{-5} to 10^{-6} mbar. Then, the metal is placed in a tungsten spiral boat that can withstand extremely high temperatures and the current is gradually increased to heat the boat resistively. The thickness of the deposited material substance is evaluated using a quartz crystal monitor. The deposition rate is normally kept as low as possible. A shutter is also included, which is used to regulate the rate at which materials are deposited on the substrate.

4. RESULTS AND DISCUSSION

4.1 Crystal Structure Analysis

The crystalline structure of the Gd_2O_3 films can have a significant influence on the dielectric properties. Therefore, different XRD, SEM, and FTIR investigations were used to figure out the crystal structure of Gd_2O_3 films.

For the determination of the crystal structure and orientation of the Gd_2O_3 First, XRD measurements were carried out on layers. Based on known data for lattice constants and atomic positions of different crystal structures [57, 58], the observed reflections are also included identified using the Vesta software [59]. Only a few weak extra reflections may be visible in the diffraction pattern in addition to the substrate reflections (Figure 4.1.) [60, 61]. The XRD measurement of the Gd_2O_3 layer shows a broad peak at $2\theta \approx 28.68^{\circ}$. This reflection can be assigned to the 222-reflection plan of cubic Gd_2O_3, while the peak at $2\theta \approx 33.2^{\circ}$ is assigned to the (400)-reflection plan of cubic Gd_2O_3, suggesting a (222) orientation of the deposited. The symmetrical 2θ measurement of the Gd_2O_3 layer shows a broad reflection at $2\theta \approx 30.8^{\circ}$. Due to very comparable 2 values having very similar crystal structures in the out-of-plane direction, the reflex is close to the monoclinic 402M or hexagonal 0002H reflex [62]. The symmetrical 2θ measurement makes it impossible to distinguish between hexagonal and monoclinic crystal structures. The arrangement of the atoms in the monoclinic and hexagonal crystal structure, however, differs significantly in the azimuthal direction, i.e., H perpendicular for (0001) or $(11\bar{2}0)$ orientation. Therefore, the investigation could give information about the real structure from asymmetrical reflexes. However, in the investigations in the area of the hexagonal asymmetrical reflex 1011H or the equivalent monoclinic reflexes, no intensity was shown [63].

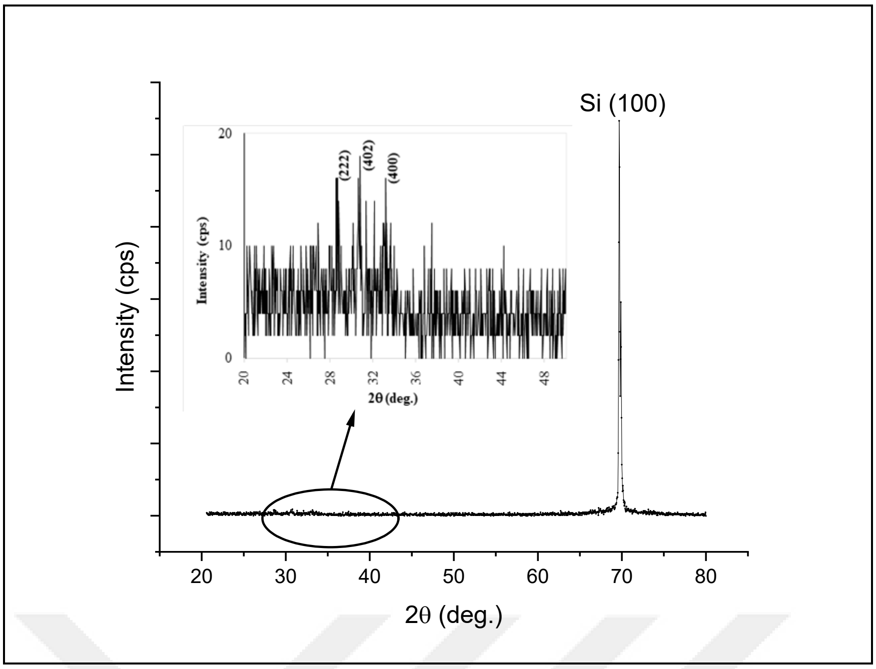

Figure 4.1. XRD measurement in symmetrical 2θ geometry of the Gd_2O_3 layers grown.

In addition, the surface morphology of the Gd_2O_3 layers was identified with AFM investigations 3D images with a size of 500 x 500 nm scanning area, the results of which are shown in Figure 4.2. The surface structure of all AFM pictures is identical almost, with minute nanorods particles on the surface with a diameter of a few nanometers. The root mean square (RMS) roughness is in the range of 5-20 nm, which is small. The mobility of atoms on the surface and other kinetic factors seems to be decisive for the formation of the different crystal structures. The surface shape of the developed Gd_2O_3 layers appears to be influenced by the laser's energy. The particle size of Gd_2O_3 decreases as the laser energy is increased. It is clear to us by the AFM image of the 900 mJ Gd_2O_3 film's that it has a flat surface with a roughness of 4.01 nm, indicating an amorphous formation. The attached Table.4.1. This demonstrates that the roughness value of the film decreased from 13.5 to 4.01 nm as the particle size decreased, which is inversely related to the increase in laser energy [64].

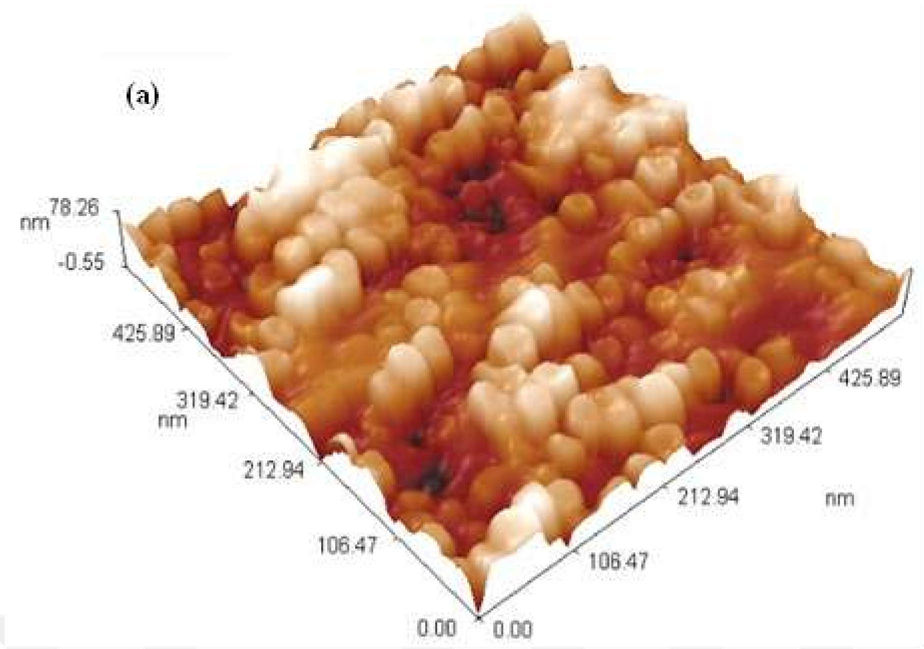

(a)
nm
78.26
-0.55
425.89
319.42
nm
212.94
106.47
0.00
0.00
106.47
212.94
319.42
425.89
nm

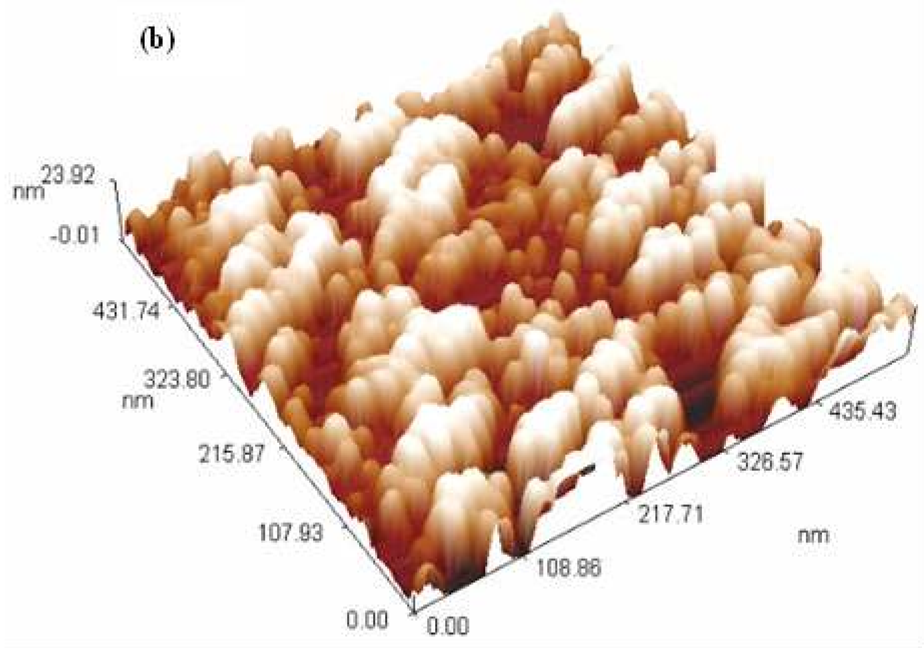

(b)
nm
23.92
-0.01
431.74
323.80
nm
215.87
107.93
0.00
0.00
108.86
217.71
326.57
435.43
nm

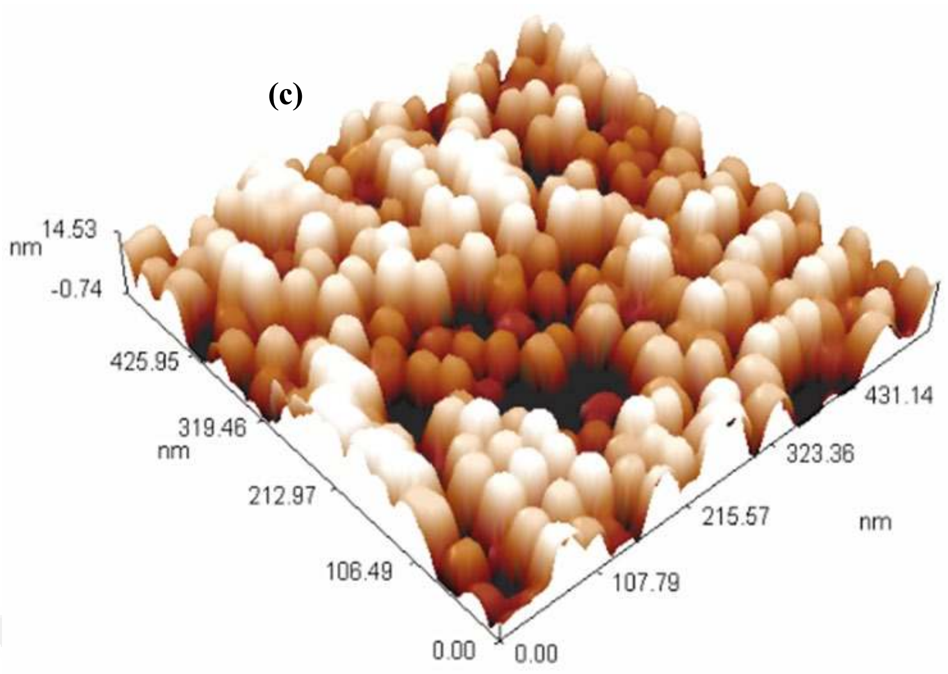

Figure 4.2. AFM images of the Gd_2O_3 layers using three different energies of the laser, 500 mJ (a), 700 mJ (b), and 900 mJ (c).

A decrease in the size of the particles was observed with the increase in the laser energy as shown in Table.4.1 and this can be explained by a decrease in the sedimentation rate of atoms, therefore, the growth rate of particle size is reduced.

Table 4.1 The average diameter is a function of laser energy.

Laser energy (mJ)	Ave. diameter (nm)	Ave. roughness (nm)	RMS (nm)
500	32.75	13.5	16.4
700	25.50	6.12	7.01
900	22.12	4.01	4.67

The Gd_2O_3 films thickened were estimated and shown in Table 4.2 using a spectroscopic reflectometer from (Angstrom solar Technologies. Inc). As the increasing laser energy delivered towards the target rose, the thickness of the layers deposited on the silicon wafer dropped. This is most likely due to the fact that when laser energy raises the temperature on the film, a chemical reaction occurs, preventing the development of big particle aggregates on the Si wafer and thereby lowering the film thickness.

Table 4.2. The film thickness vs the increase in laser energy.

Laser energy (mJ)	Film thickness (nm)
500	110
600	83
700	47
800	41
900	34

For further investigation of the layer and crystal structure were Scanning electron microscopy (SEM) recordings were carried out, which are shown in Figure 4.3. The SEM image confirms the existence of sample particles of Gd_2O_3 with sizes (30 to 500 nm).

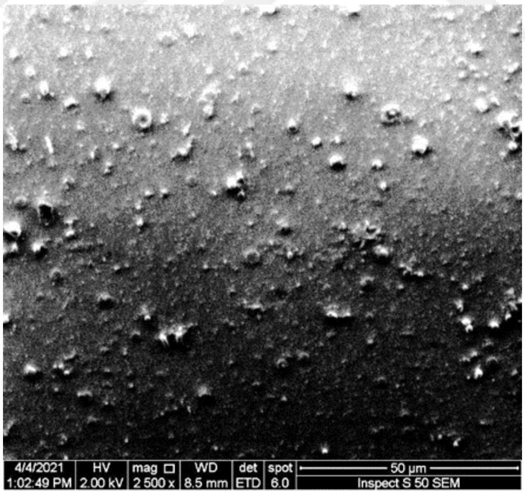

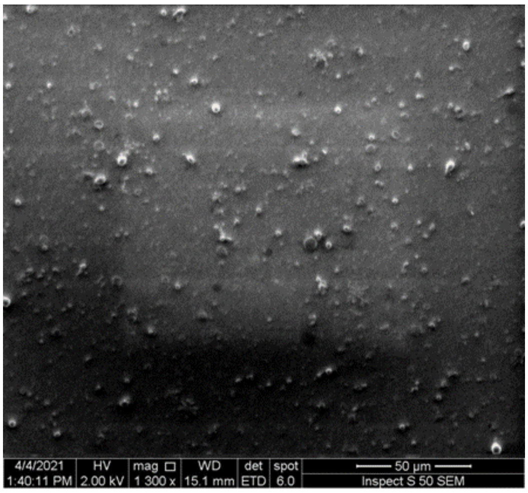

Figure 4.3. SEM images of the Gd_2O_3 thin film deposited on the p-Si substrate.

4.2 Optical Properties of Gd_2O_3/Si

A UV-Vis spectrophotometer (Shimadzu. UV-310PC) was used to measure absorbance in the wavelength range of 300-1100 nm at room temperature, to calculate the bandgap of the deposited films. The UV-Vis transmission spectra of Gd_2O_3 films formed on glass using various laser energies are shown in Figure 4.4. The average transmittance of samples decreases with wavelength. The bandgap values ranged from 3.10 to 3.46 eV as in Table 4.3. The optical band gap value for Gd_2O_3 has been calculated to be $Eg \approx 5.62$ eV [65], which is significantly larger than the value calculated here.

Films deposited on glass show strong absorption at ~ 290 nm and the highest bandgap value ~3.46 eV obtained for a Gd_2O_3 film deposited with laser energy of 800 mJ. As a result of the annealing process, the bandgap is minimized. Because the amount of Gd_2O_3 deposited can be controlled by the laser intensity during deposition, the bandgap may be altered.

The transmission spectra were calculated using the formula at the optical absorption band's edge area $\alpha hv = A(E_g - hv)^2$ where $\alpha = ln(100/T)/d$. It may be feasible to fit sections of the $\alpha hv = f(hv)$ curves to one or more standard dependencies [66], for which the best fit was found in the empirical analysis for the $(\alpha hv)^2 = f(hv)$ curves.

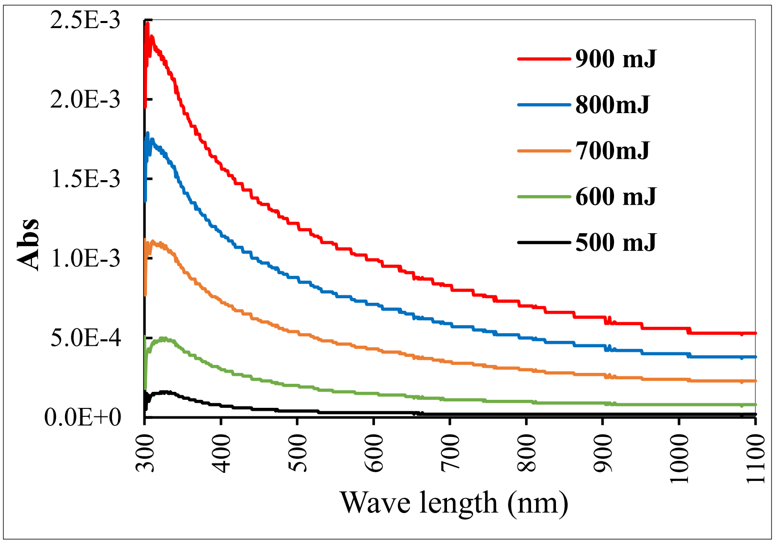
Abs
2.5E-3
2.0E-3
1.5E-3
1.0E-3
5.0E-4
0.0E+0
300
400
500
600
700
800
900
1000
1100
Wave length (nm)
900 mJ
800mJ
700mJ
600 mJ
500 mJ

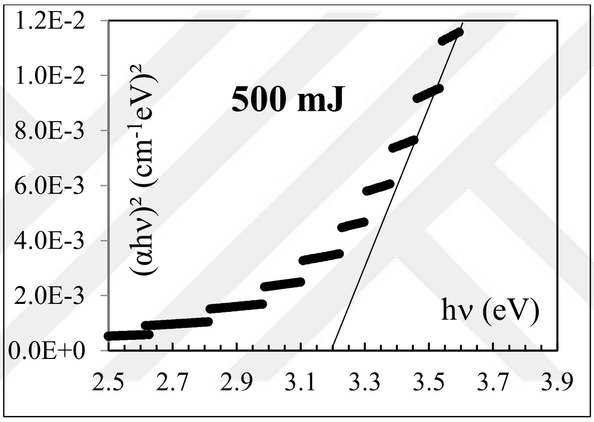
500 mJ
(αhν)² (cm⁻¹eV)²
hν (eV)
1.2E-2
1.0E-2
8.0E-3
6.0E-3
4.0E-3
2.0E-3
0.0E+0
2.5
2.7
2.9
3.1
3.3
3.5
3.7
3.9

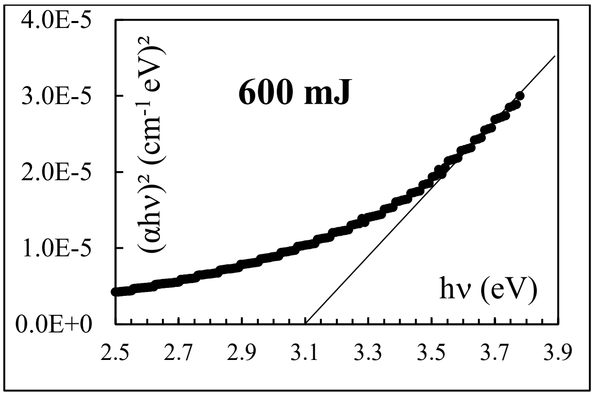
600 mJ
(αhν)² (cm⁻¹ eV)²
hν (eV)
4.0E-5
3.0E-5
2.0E-5
1.0E-5
0.0E+0
2.5
2.7
2.9
3.1
3.3
3.5
3.7
3.9

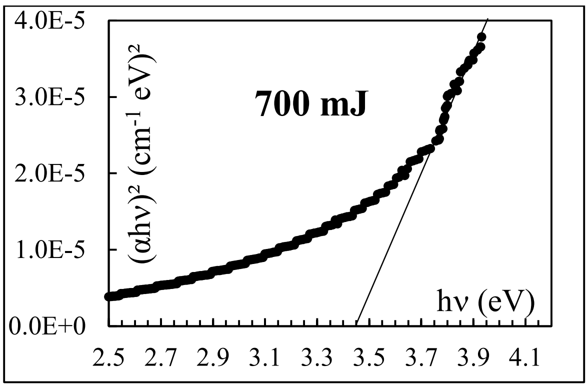
700 mJ
(αhν)² (cm⁻¹ eV)²
hν (eV)
4.0E-5
3.0E-5
2.0E-5
1.0E-5
0.0E+0
2.5
2.7
2.9
3.1
3.3
3.5
3.7
3.9
4.1

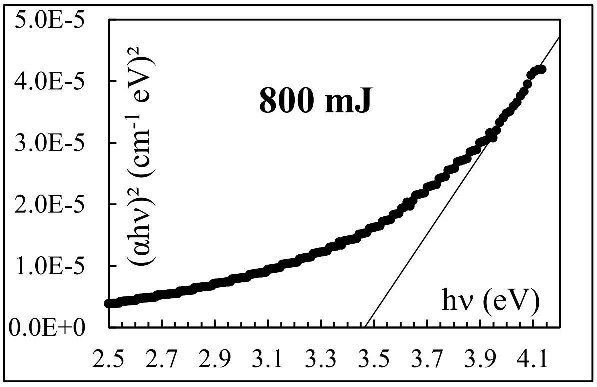

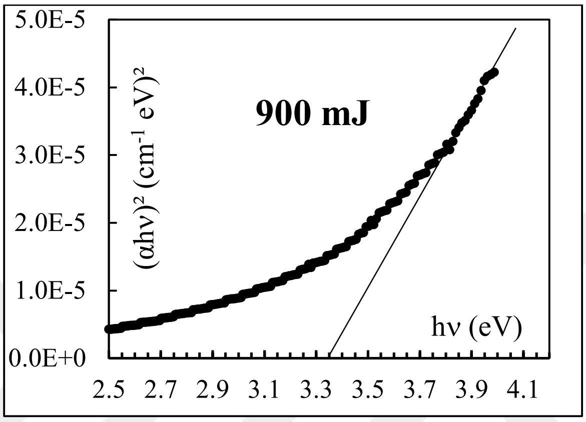

Figure 4.4. The optical absorption spectrum and corresponding bandgap for different films were obtained using different laser energy.

Table 4.3. The average band gap of the deposited film is a function of laser energy.

Lase energy (mJ)	**Energy gap (eV)**
500	3.20
600	3.10
700	3.45
800	3.46
900	3.35

4.3 FTIR Analysis

The IR spectra of the deposited structures were recorded using a Bruker Vertex 70 FT-IR spectrometer Hyperion 3000 microscope with 15x magnification taken in reflection. The aim of the investigation was to collect information about the presence or absence of the oxygen anion in the precipitated salt as well as any notes on the oxide and hydroxide content of the samples. During the measurement, the spectra shown in Figures 4.5.a to d are made of Gd_2O_3 deposited on the substrate. When looking at the spectra, the broad peak in the area around is noticeable, this is with the spectrum of the Gd_2O_3 deposited using low energy laser, the peak is visible at 1880 cm^{-1} for all spectra. Further a small peak fall in the area around 1700 cm^{-1} as well as a more pronounced peak at 1640 cm^{-1} using low laser energy, which is present in all samples. In the wider wave number range below 1600 cm^{-1} all spectra differ greatly from one another. New peaks at 548 and 455 cm^{-1} in the cubic Gd_2O_3 phase may be ascribed to Gd-O vibrations, indicating the formation of polycrystalline Gd_2O_3 films. Valleys at 748 and 610 cm^{-1} are connected with crystalline Si vibrational modes. Because of the interaction of Si with O in the air, the absorption bands exhibit aggregates of Si-O at 1109 and 1059 cm^{-1}, which fluctuate with the increase in laser energy used for deposition. Bonding arrangements at silicon atomic sites are statistically distributed in a variety of ways. The silicon substrate surface can explain the apparent broadening of these peaks, since this may result in varied bond angle and bond length values. It is noteworthy that the Si-O and Gd-O bands are visible simultaneously, showing that the production of Gd_2O_3 films promotes oxygen transport and Si-O bonds are formed when Si and O are combined. This suggests that Gd_2O_3 membranes can operate as a catalyst for the creation of atomic oxygen, which diffuses quickly across the film and leads to the formation of interfacial silicon oxide layers owing to oxygen ion conduction [67].

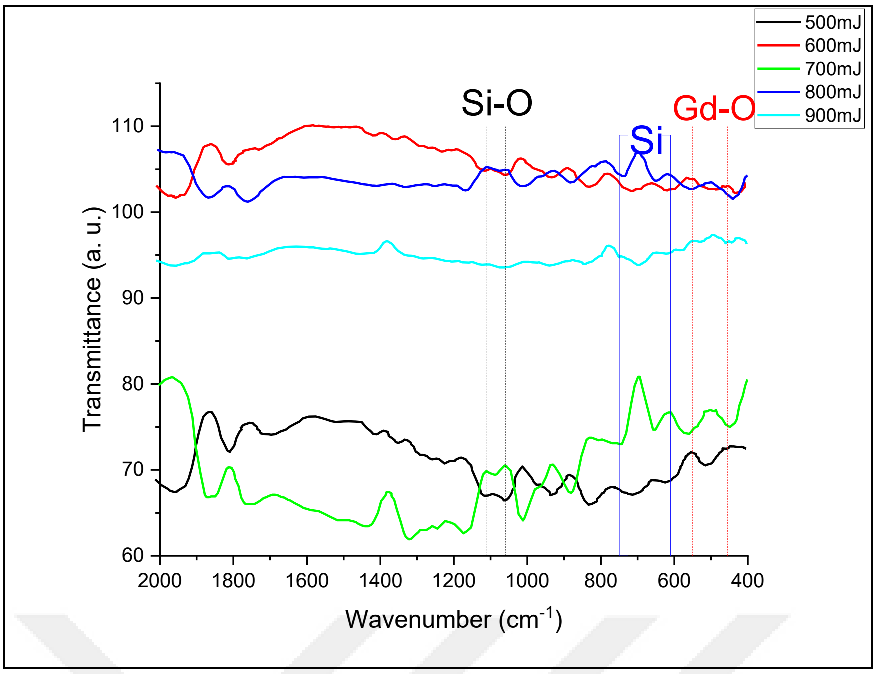

Figure 4.5. FT-IR spectrum for Gd_2O_3/Si.

4.4 Current-Voltage Measurements of Gd_2O_3/Si

In theory, an ideal insulator does not conduct electricity. In real form, however, a current flow cannot be completely avoided in any isolator. The flow of current through an isolator can be many different processes be responsible. The resulting current flow through the isolator is referred to as leakage current and its size is a measure of the quality and applicability of the dielectric layers. The following section describes the Gd_2O_3 layers characterized from this work with current-voltage measurements to emphasize the behavior of leakage currents and other electrical features. The I-V measurements of the differently manufactured Gd_2O_3 films using different laser power were depleted. Through oxide, all curves show a normal one leakage current behavior on the right side of the chart, with merely a smidgeon of an increased semi-logarithmic representation at the beginning of the curve can be seen. All curves have a steeper rise above a certain voltage of the curve, suggesting a change in the predominant charge transport mechanism.

When the negative voltage is raised to 5 V, as shown in Figure 4.6(a, b, d), there is essentially no leakage current (< 10^{-9} A). As the negative voltage was increased to 5 V in Figure 4.6(c, e), however, leakage currents of ~1 to 1.2 μA were found, with decreasing defect densities in the oxide for different films, the typical leakage current density is reduced for films of comparable thickness. Flaw-assisted tunneling is determined by the density of defects in the oxide, is a charge transport method in high-k materials [68, 69]. Defect-assisted tunneling in Gd_2O_3 film in Gd_2O_3 /(CZ-pSi) diodes has already been considered as the predominant charge transport mechanism drawn [70]. The reduction in the defect density can therefore be the reason behind the decrease in typical leakage current densities, where the defects are traps for charge carriers. Compared to cubic Gd_2O_3, the Gd_2O_3 layer's leakage current densities have decreased compared to that produced using low laser power [71, 72]. Furthermore, the presence of crystalline domains in cubic Gd_2O_3 was observed to cause an increase in leakage current in CET > 1 nm layers, as domain boundaries can act as current leakage paths [71]. In contrast, the layers in this study should have more domains and thus more domain boundaries that can act as leakage current paths. Surprisingly, when compared to double-domain cubic Gd_2O_3 with identical CET values, they have characteristic leakage current densities in the same range or even lower. This indicates that charge transmission across domain boundaries is not the primary mode of transport here. Furthermore, different charge transport mechanisms of the Gd_2O_3-films were examined with different I-V measurements and evaluations. The measurements were carried out on Gd_2O_3 films integrated into Gd_2O_3/(CZ-pSi) diodes. Lipp et al. suspect when examining Gd_2O_3/(CZ-pSi) diodes with cubic Gd_2O_3 that the particular barrier height does not create a difference between the metal's Fermi energy and the oxide's conduction band edge, but only the difference to a defect level through which the charge transport takes place [70]. Such a scenario would also be conceivable for layers from this work. As a consequence, due to their low leakage current in the voltage range of -5 to 0.5 V, Gd_2O_3/(CZ-pSi) diode for energies 500, 600, and 800 mJ might be regarded as important candidate detectors. Therefore, Gd_2O_3/(CZ-pSi) diode for energy 500 mJ was selected for testing as a detector after gamma rays were irradiated on it, the results of which are presented later in our study.

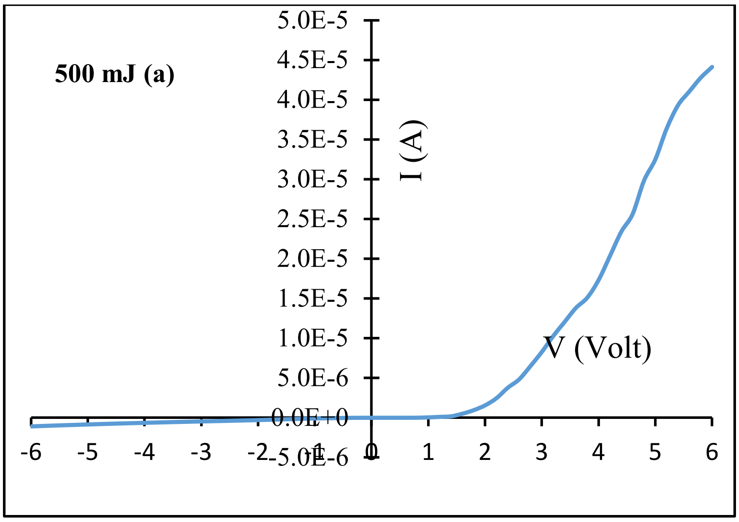
500 mJ (a)
I (A)
V (Volt)
5.0E-5
4.5E-5
4.0E-5
3.5E-5
3.0E-5
2.5E-5
2.0E-5
1.5E-5
1.0E-5
5.0E-6
0.0E+0
-5.0E-6
-6 -5 -4 -3 -2 -1 0 1 2 3 4 5 6

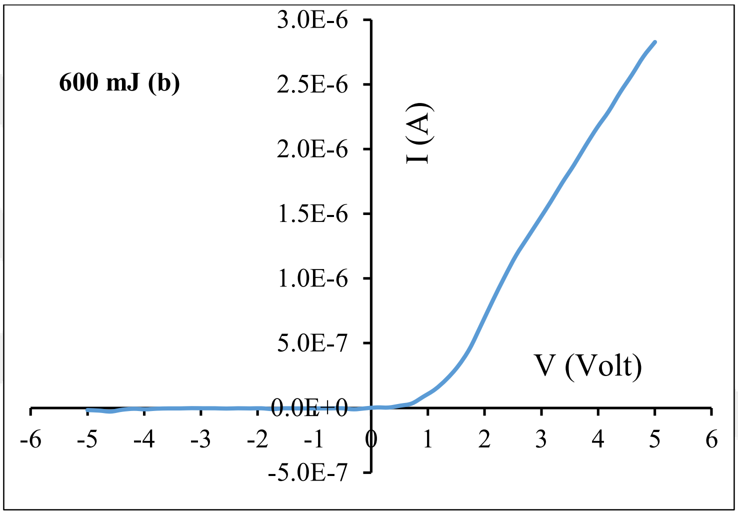
600 mJ (b)
I (A)
V (Volt)
3.0E-6
2.5E-6
2.0E-6
1.5E-6
1.0E-6
5.0E-7
0.0E+0
-5.0E-7
-6 -5 -4 -3 -2 -1 0 1 2 3 4 5 6

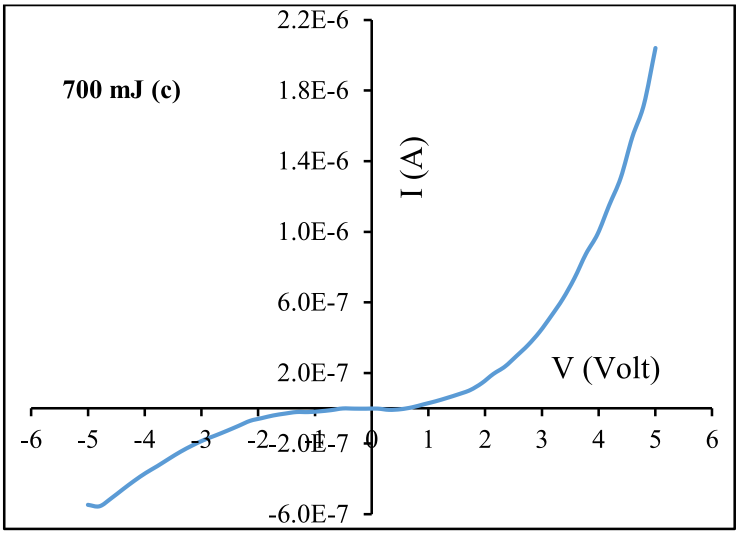
700 mJ (c)
I (A)
V (Volt)
2.2E-6
1.8E-6
1.4E-6
1.0E-6
6.0E-7
2.0E-7
-2.0E-7
-6.0E-7
-6 -5 -4 -3 -2 -1 0 1 2 3 4 5 6

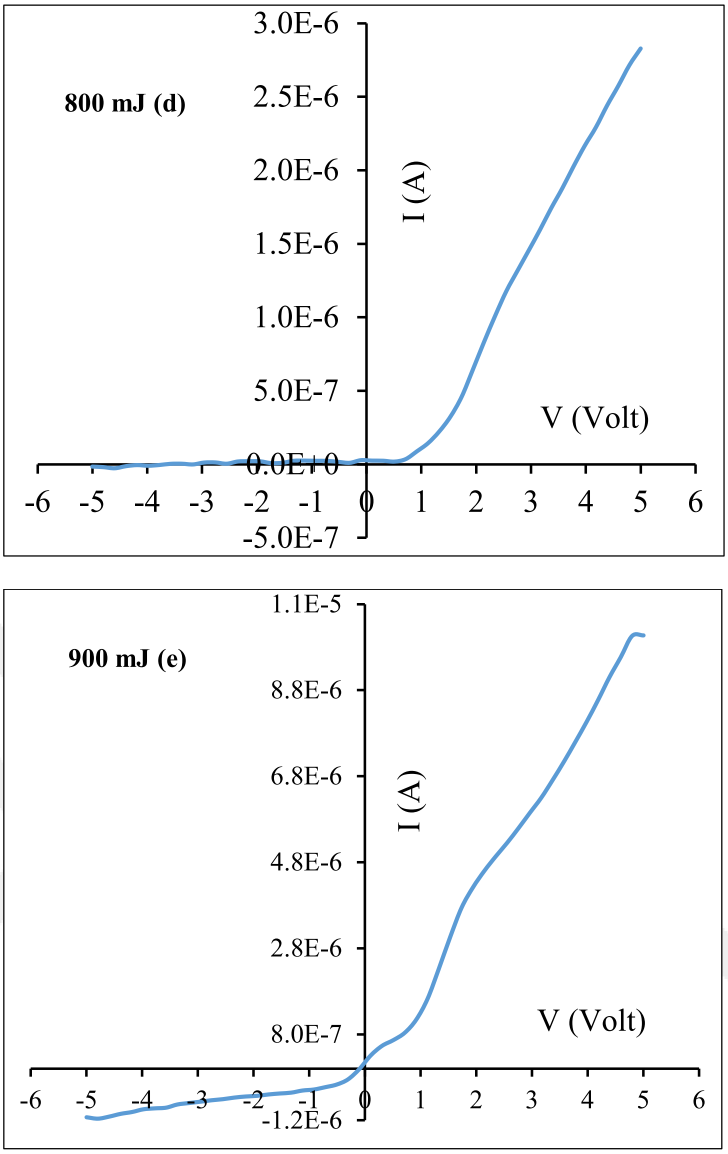

Figure 4.6. I-V measurements of the leakage current of Gd_2O_3/(CZ-pSi) diodes.

4.5 Capacitance-Voltage Measurements of Gd_2O_3/Si

When measuring C-V to determine the characteristics of Gd_2O_3/(CZ-pSi) diodes deposited with various laser energies at frequencies ranging from 10 to 1000 kHz, it was discovered that all of the samples' curves were dependent on the voltage and frequency, as shown in Figure 4.7.

The lifetime of the interface states between Gd_2O_3 and the silicon substrate was discovered to be one of the most important parameters, resulting in capacitance variations at different frequencies. The frequency-dependent interfacial capacitance is apparently formed by the interfacial state modulation induced by the AC signal at low frequencies of 300 kHz and below.

Because the interface states do not have enough time to follow the AC signal at high frequencies of 500 kHz and higher, their contribution to total capacitance is similarly reduced.

The results obtained showed that the C-V characteristics of Gd_2O_3/(CZ-pSi) diodes are inversely proportional to the increase in frequency [73].

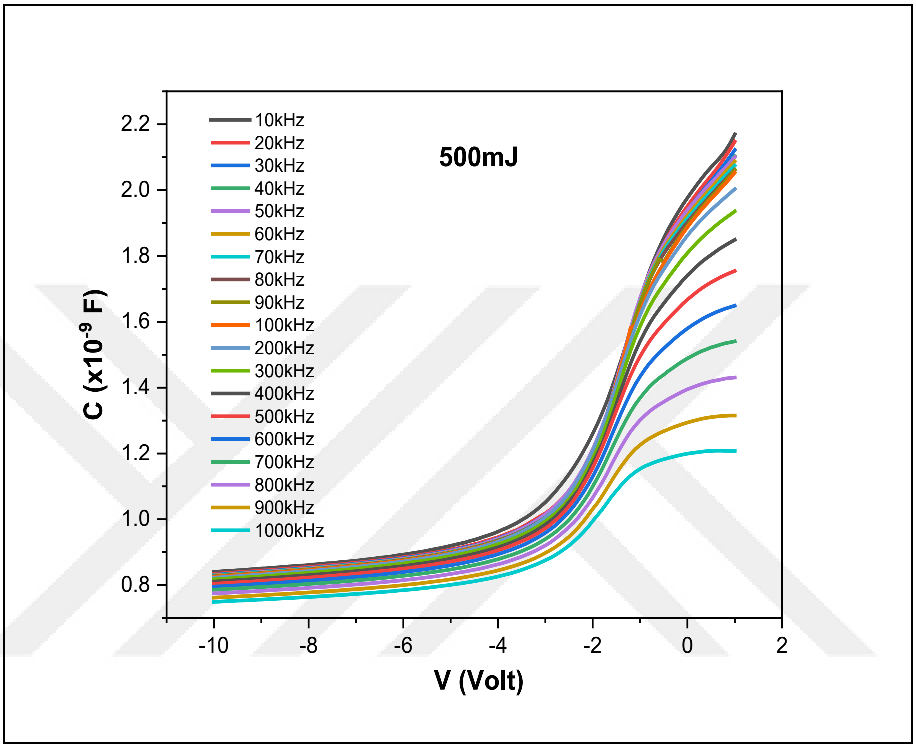

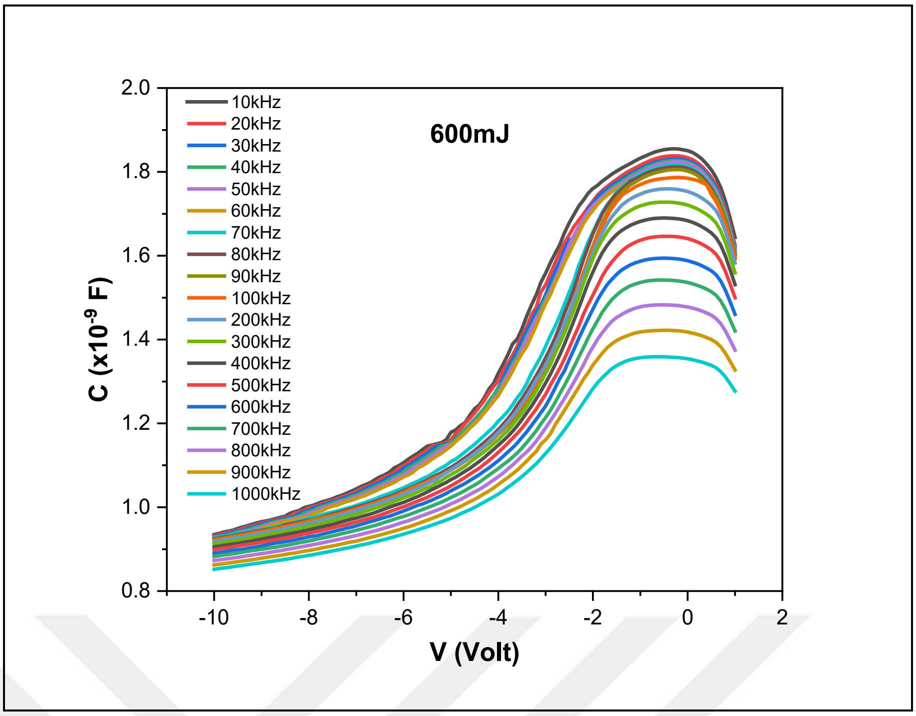
600mJ
C (x10-9 F)
V (Volt)
10kHz
20kHz
30kHz
40kHz
50kHz
60kHz
70kHz
80kHz
90kHz
100kHz
200kHz
300kHz
400kHz
500kHz
600kHz
700kHz
800kHz
900kHz
1000kHz

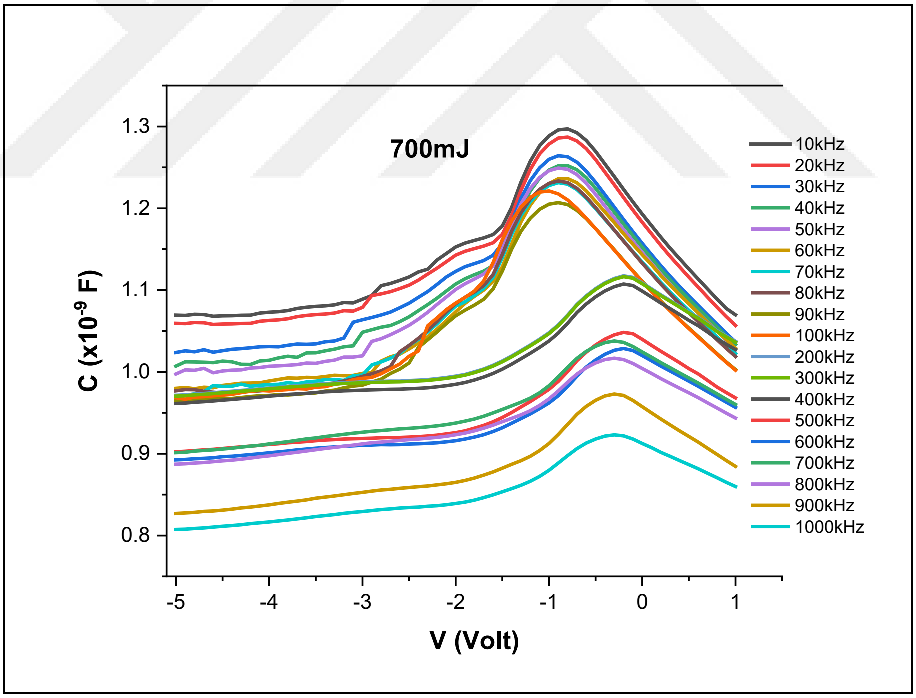
700mJ
C (x10-9 F)
V (Volt)
10kHz
20kHz
30kHz
40kHz
50kHz
60kHz
70kHz
80kHz
90kHz
100kHz
200kHz
300kHz
400kHz
500kHz
600kHz
700kHz
800kHz
900kHz
1000kHz

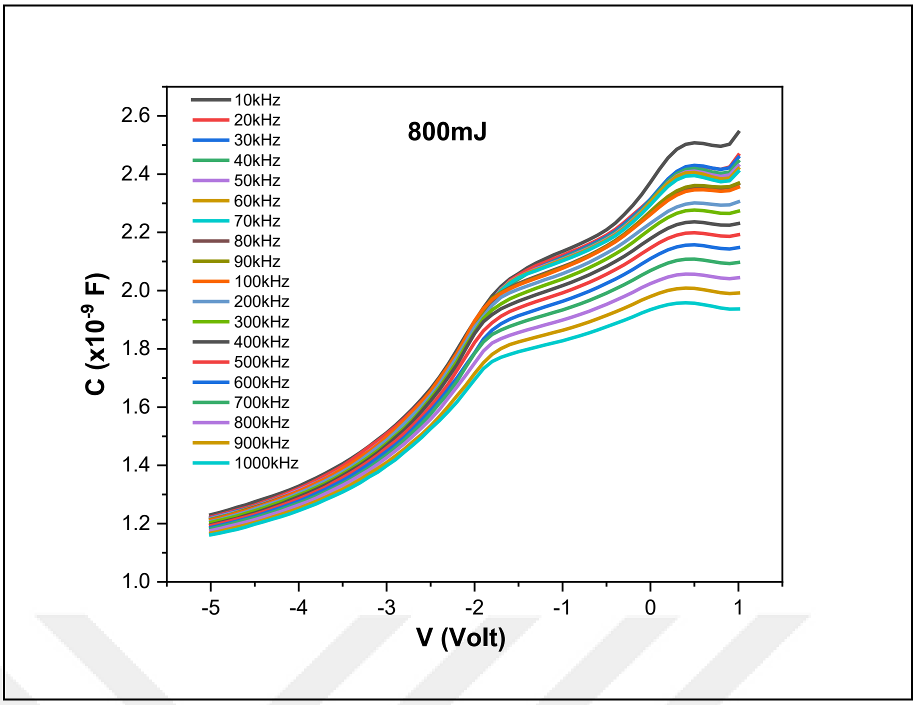

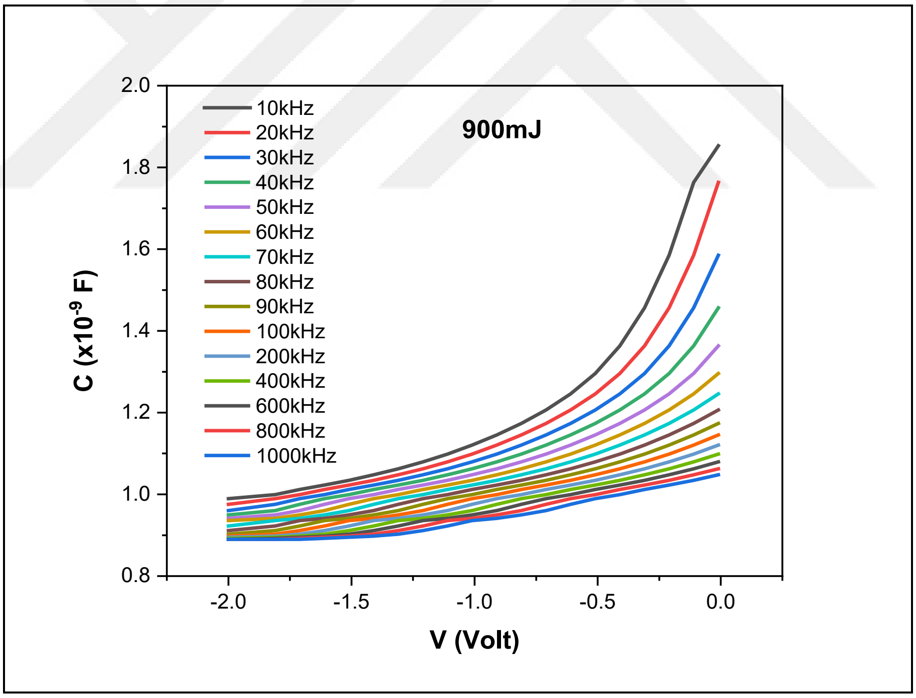

Figure 4.7. C-V measurements of the Gd_2O_3 films.

We can get data from the diodes because of the carrier discrepancies between the layers. The capacitance of the Gd_2O_3/(CZ-pSi) diode decreases with reverse voltage, as seen in Figure 4.8. The diode is stable at negative voltages in the entirely depleted Gd_2O_3 area, where the carrier concentration may be lower, according to the C-V curves. The V axis is derived from the slope $1/C^2$ curve. Because they are less than 2, these results are promising because they allow the diode to switch on at low voltages without losing function. They can be employed as neutron/alpha detectors if the carrier concentrations are low enough, as determined by the $1/C^2$ slope.

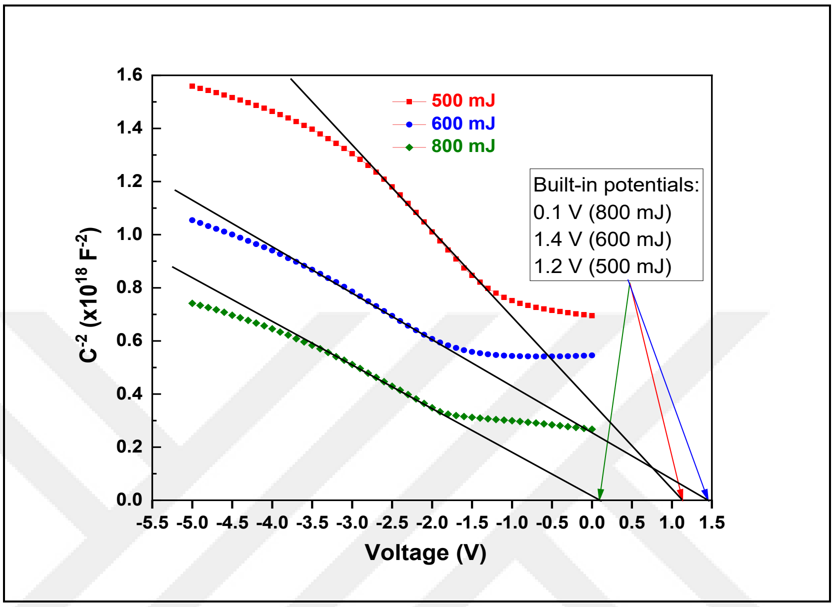

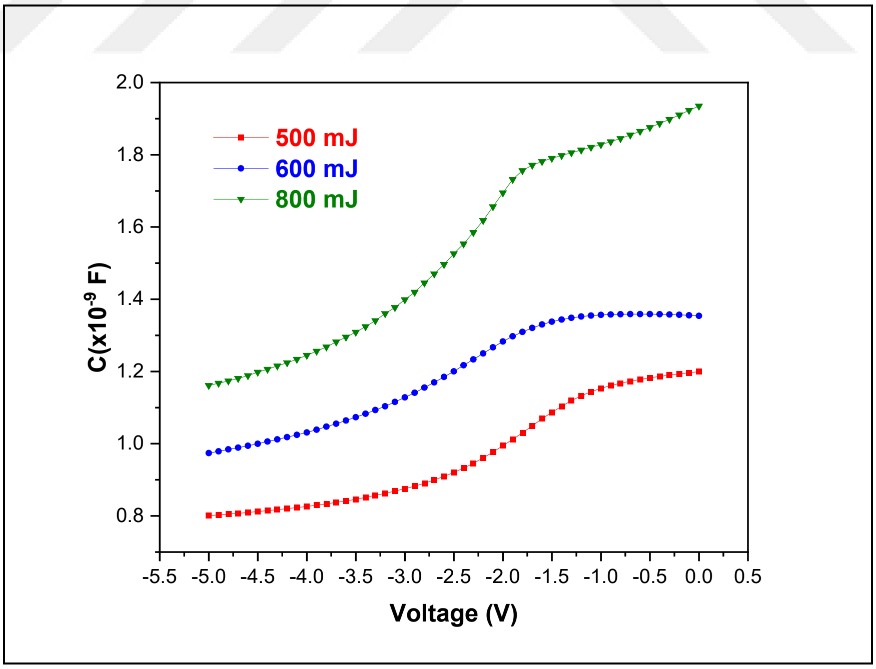

Figure 4.8. (C-V, left) and ($1/C^2$-V, right) curves of the best diodes precipitated with energies (500, 600, 800 mJ).

4.6 Evaluation of I-V Measurements of Gd_2O_3/Si Under Radiation

In Figure 4.9, which represents the diagram of the current-voltage relationship for a Gd_2O_3/(CZ-pSi) diode that deposits a 500 mJ laser energy after being exposed to gamma rays at a dose rate of (0-50 Gy) at a frequency of (100 kHz), the current begins to decrease with an increasing dose of gamma rays and when we continue to give more doses of gamma rays, the current may drop so much that it approaches zero, according to literature data [74], This suggests that radiation has a significant impact on Gd_2O_3/(CZ-pSi) diodes. The current diminishes because the produced interfacial traps are mostly ionic oxygen vacancy defects, which are full of radiation damaging effects.

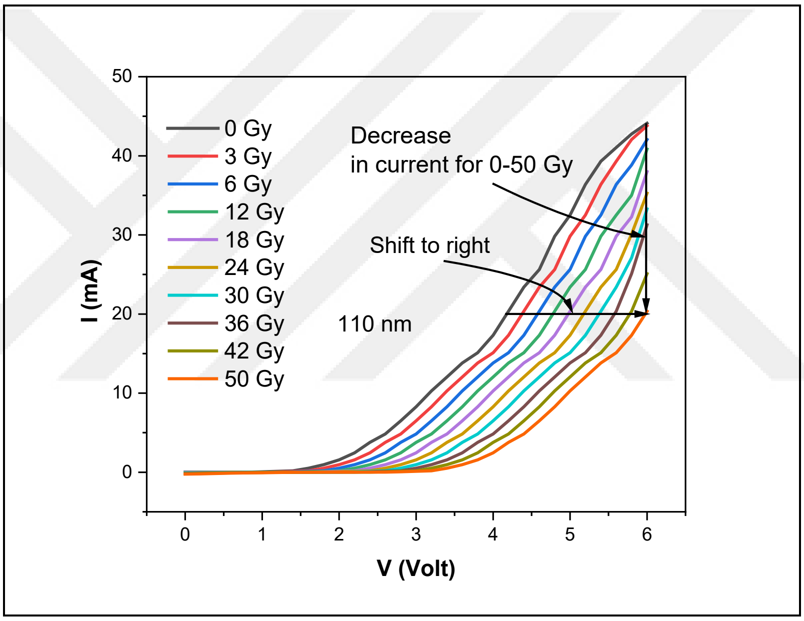

Figure 4.9. I-V measurements for Gd_2O_3 films under the influence of gamma-ray.

4.7 Evaluation of C-V Measurements of Gd_2O_3/Si Under Radiation

After irradiating different doses of gamma rays (3, 6, 12, 18, 24, 30, 36, 42 and 50 Gy) on a thin film of Gd_2O_3 deposited using 500 mJ laser energy and repeating the CV measurements, the electrical parameters changed in the frequency of 100 kHz, found the transition of the curve to the right side of the curve before irradiation as their capacitance increased over the voltage range -1 V to 10 V, which continues to increase with the consumption of voltage. When checking the extent of the changes, it is clear after comparing between 0 and 50 Gy radiation dose, a significant increase in capacitance, which is 1.19 – 2 nF at a voltage of 2 V. The charge trapped at the interface and its distribution along the bandgap has a significant influence on semiconductor-based device responsiveness [75].

After irradiation, the Al/Gd_2O_3/(CZ-pSi)/Al diode performed well. In contrast to the drop in current, the capacity of the film did not decrease when it was irradiated but rather increased. Over the dosage range studied, corrected oxide capacitances ranged from 2.06 nF to 2.19 nF for all diodes. Radiation-induced interfacial traps alter the radiation behavior of Al/Gd_2O_3/(CZ-pSi)/Al diodes. The most prevalent ionic defects in Gd_2O_3 formed on silicon are oxygen vacancies. The sensitivity value was determined to be 44.8 ±2.9 mV/Gy, for a total exposure of 50 Gy, which is higher than that of conventional SiO_2 based MOS devices in compliance with the literature data [76].

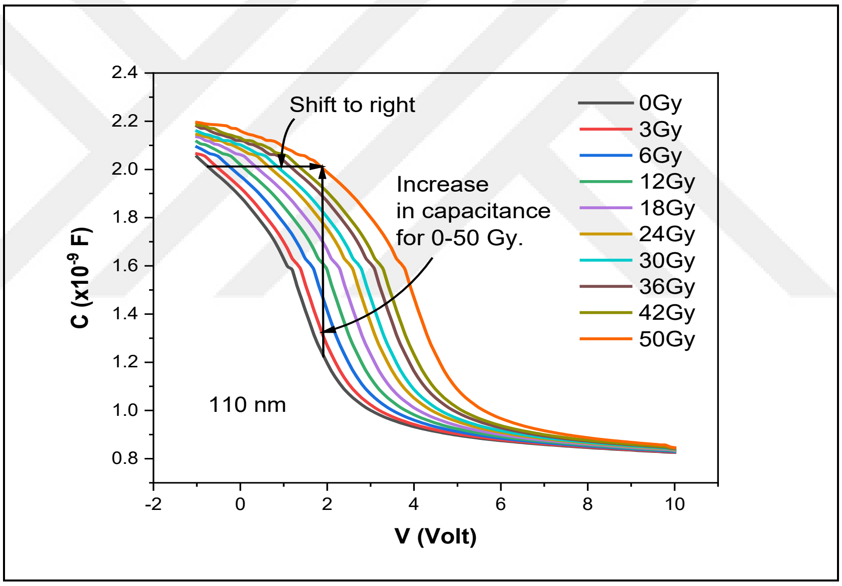

Figure 4.10. C-V measurements for Gd_2O_3 films under the influence of gamma-ray.

5. CONCLUSIONS AND RECOMMENDATIONS

In this study, the fabrication of Al/Gd_2O_3/(CZ-pSi)/Al diodes and evaluation of its structural, electrical parameters under radiation and the sensitivity of high-k oxides to radiation is inspected. Several samples were fabricated from the Al/Gd_2O_3/(CZ-pSi)/Al diodes consisting of a thin n-type layer of Gd_2O_3 deposited on CZ silicon wafers p-type (100) and glass substrates at different laser energies 500 to 900 mJ at room temperature and pressure 3.3×10^{-2} Pa by the pulsed laser deposition technique (PLD).

It was originally noticed that as the laser power aimed at the target increased, the layer thickness and particle size deposited on silicon wafers dropped. C-V measurements were taken for all diodes in the frequency range of electrical characteristics from 10 to 1000 kHz, and a drop was seen with increasing frequency. We concluded after irradiating the Gd_2O_3 films deposited using 500 mJ laser energy with different doses of gamma rays, which was 3 to 50 Gy having a change in its electrical evaluation parameter by repeating the electrical measurements, it was found that C-V measurements at various frequencies ranging at a frequency of 100 kHz showed a shift of the curves to the right of the pre-radiation curves, which continues and increases with increasing radiation dose. Also, the effect of I-V measurements was shown, which showed a shift of the current curves, which started decreasing with the increase of the radiation dose and which continues to decrease with the increase of the radiation dose to the point that it approaches zero. The corrected capacitance of the top oxide rises from 2.05 to 2.19 nF when the dose varies from 0 to 50 Gy, as illustrated in Figure 4.10. This was noticed across the board for all diodes. A particular sensitivity value of 44.8 ±2.9 mV/Gy was established for a dosage of 50 Gy. Depending on the construction laser energy of the Gd_2O_3 layer, band gaps in the range of 3.10 to 3.46 eV may be obtained for Gd_2O_3 deposited on glass.

Therefore, I find it interesting in future research to know the frequency dependence of the electrical and optical responses of Gd_2O_3 devices fabricated using floating zone (FZ-pSi) technology before and after irradiation, as well as the use of pulsed laser deposition technique (PLD) using low laser energies.

6. REFERENCES

"Vancouver citation system was used in this thesis."

1. Frank DJ, Dennard RH, Nowak E, Solomon PM, Taur Y, Wong HS. Device scaling limits of Si MOSFETs and their application dependencies. Proceedings of the IEEE. 2001 Mar;89(3):259-88.

2. Stathis JH. Reliability limits for the gate insulator in CMOS technology. IBM Journal of Research and Development. 2002 Mar;46(2.3):265-86.

3. Ning, T., Silicon technology directions in the new millennium. 2000. 1-6.

4. Nakajima A, Khosru QD, Yoshimoto T, Kidera T, Yokoyama S. NH 3-annealed atomic-layer-deposited silicon nitride as a high-k gate dielectric with high reliability. Applied Physics Letters. 2002 Feb 18;80(7):1252-4.

5. Desbiens E, Dolbec R, El Khakani MA. Reactive pulsed laser deposition of high-k silicon dioxide and silicon oxynitride thin films for gate-dielectric applications. Journal of Vacuum Science & Technology A: Vacuum, Surfaces, and Films. 2002 May;20(3):1157-61.

6. Wong H, Zhan N, Ng KL, Poon MC, Kok CW. Interface and oxide traps in high- κ hafnium oxide films. Thin Solid Films. 2004 Sep 1;462:96-100.

7. Jeon IS, Park J, Eom D, Hwang CS, Kim HJ, Park CJ, Cho HY, Lee JH, Lee NI, Kang HK. Investigation of interface trap states in TiN/Al_2O_3/p-Si capacitor by deep level transient spectroscopy. Applied physics letters. 2003 Feb 17;82(7):1066-8.

8. Youm M, Sim HS, Jeon H, Kim SI, Kim YT. Metal oxide semiconductor field effect transistor characteristics with iridium gate electrode on atomic layer deposited ZrO2 high-k dielectrics. Japanese journal of applied physics. 2003 Aug 1;42(8R):5010.

9. Paily R, DasGupta A, DasGupta N, Bhattacharya P, Misra P, Ganguli T, Kukreja LM, Balamurugan AK, Rajagopalan S, Tyagi AK. Pulsed laser deposition of TiO2 for MOS gate dielectric. Applied Surface Science. 2002 Feb 28;187(3-4):297-304.

10. Jing-Chi, Y., B.C. Lai, and J.Y. Lee, Fabrication and characterization of metal-oxide-semiconductor field-effect transistors and gated diodes using Ta_2O_5/ gate oxide. IEEE Electron Device Letters, 2000. 21(11): p. 537-539.

11. Hubbard KJ, Schloma DG. Thermodynamic Stability of Binary Oxides in Contact with Silicon. MRS Online Proceedings Library (OPL). 1995;401.

12. Mistry K, Allen C, Auth C, Beattie B, Bergstrom D, Bost M, Brazier M, Buehler M, Cappellani A, Chau R, Choi CH. A 45nm logic technology with high-k+ metal gate transistors, strained silicon, 9 Cu interconnect layers, 193nm dry patterning, and 100% Pb-free packaging. In2007 IEEE International Electron Devices Meeting 2007 Dec 10, pp. 247-250. IEEE.

13. Wilk GD, Wallace RM, Anthony J. High- κ gate dielectrics: Current status and materials properties considerations. Journal of applied physics. 2001 May 15;89(10):5243-75.

14. Robertson J. High dielectric constant gate oxides for metal oxide Si transistors. Reports on progress in Physics. 2005 Dec 14;69(2):327.

15. Ribes G, Mitard J, Denais M, Bruyere S, Monsieur F, Parthasarathy C, Vincent E, Ghibaudo G. Review on high-k dielectrics reliability issues. IEEE Transactions on Device and materials Reliability. 2005 Jun 13;5(1):5-19.

16. Jung HS, Ryu JT, Kim DH, Kim TW. Mobility degradation mechanisms of MOSFETs with a high-k dielectric layer. Journal of Nanoscience and Nanotechnology. 2014 Nov 1;14(11):8215-8.

17. Zhu W, Han JP, Ma TP. Mobility measurement and degradation mechanisms of MOSFETs made with ultrathin high-k dielectrics. IEEE Transactions on Electron Devices. 2004 Jan 7;51(1):98-105.

18. Huang A, Zheng X, Xiao Z, Wang M, Di Z, Chu PK. Interface dipole engineering in metal gate/high-k stacks. Chinese Science Bulletin. 2012 Aug;57(22):2872-8.

19. Charalampides G, Vatalis KI, Apostoplos B, Ploutarch-Nikolas B. Rare earth elements: industrial applications and economic dependency of Europe. Procedia Economics and Finance. 2015 Jan 1;24:126-35.

20. Weber R, Tangeman JA, Nordine PC, Scheunemann RN, Hiera KJ, Ray CS. Rare earth – aluminum oxide glasses for optical applications. Journal of non-crystalline solids. 2004 Oct 15;345:359-65.

21. Wang, R. G.,Hydrothermal synthesis of rare-earth oxide Nanocatalysts for automotive exhaust clean-up, 2012. 512-515: p. 1624-1629.

22. Tanaka T, Kuzuhara M, Watada M, Oshitani M. Effect of rare earth oxide additives on the performance of NiMH batteries. Journal of alloys and compounds. 2006 Feb 9;408:323-6.

23. Azimi G, Dhiman R, Kwon HM, Paxson AT, Varanasi KK. Hydrophobicity of rare-earth oxide ceramics. Nature materials. 2013 Apr;12(4):315-20.

24. Gottlob HD, Echtermeyer T, Mollenhauer T, Efavi JK, Schmidt M, Wahlbrink T, Lemme MC, Kurz H, Czernohorsky M, Bugiel E, Osten HJ. CMOS integration of epitaxial Gd_2O_3 high-k gate dielectrics. Solid-State Electronics. 2006 Jun 1;50(6):979-85.

25. Leskel ä M, Ritala M. Rare-earth oxide thin films as gate oxides in MOSFET transistors. Journal of Solid State Chemistry. 2003 Feb 15;171(1-2):170-4.

26. Frohlich K, Luptak R, Dobrocka E, Husekova K, Cico K, Rosova A, Lukosius M, Abrutis A, Pisecny P, Espinos JP. Characterization of rare earth oxides based MOSFET gate stacks prepared by metal-organic chemical vapour deposition. Materials science in semiconductor processing. 2006 Dec 1;9(6):1065-72.

27. Zinkevich M. Thermodynamics of rare earth sesquioxides. Progress in Materials Science. 2007 May 1;52(4):597-647.

28. Gy GY, Imanaka N. The binary rare earth oxides. Chemical reviews. 1998 Jun 18;98(4):1479-514.

29. Shpil'rain, Dnk, Lsb. Investigation of fusion and phase transition enthalpies of Y_2O_3 and Sc_2O_3. Rev Int Hautes Temp Refract, 1978. 15: p. 249-252.

30. Edge LF, Tian W, Vaithyanathan V, Heeg T, Schlom D, Klenov D, Stemmer S, Wang J, Kim MJ. Growth and characterization of alternative gate dielectrics by molecular-beam epitaxy. ECS Transactions. 2008 Oct 3;16(5):213.

31. Pauling L, Shappell MD. 8. The crystal structure of bixbyite and the c-modification of the sesquioxides. Zeitschrift f ür Kristallographie-Crystalline Materials. 1930 Dec 1;75(1):128-42.

32. Osten HJ, Liu JP, Bugiel E, M üssig HJ, Zaumseil P. Growth of crystalline praseodymium oxide on silicon. Journal of crystal growth. 2002 Feb 1;235(1-4):229-34.

33. Hyde BG, Bevan DJ, Eyring L. On the praseodymium+ oxygen system. Philosophical Transactions of the Royal Society of London. Series A, Mathematical and Physical Sciences. 1966 May 19;259(1106):583-614.

34. Xiao W, Guo Q, Wang EG. Transformation of CeO2 (111) to Ce_2O_3 (0001) films. Chemical Physics Letters. 2003 Jan 24;368(5-6):527-31.

35. Mikhelashvili V, Eisenstein G, Edelman F, Brener R, Zakharov N, Werner P. Structural and electrical properties of electron beam gun evaporated Er_2O_3 insulator thin films. Journal of applied physics. 2004 Jan 15;95(2):613-20.

36. Yang H, Wang H, Luo HM, Feldmann DM, Dowden PC, DePaula RF, Jia QX. Structural and dielectric properties of epitaxial Sm_2O_3 thin films. Applied Physics Letters. 2008 Feb 11;92(6):062905.

37. Fissel A, Elassar Z, Kirfel O, Bugiel E, Czernohorsky M, Osten HJ. Interface formation during molecular beam epitaxial growth of neodymium oxide on silicon. Journal of applied Physics. 2006 Apr 1;99(7):074105.

38. Osten HJ, Laha A, Czernohorsky M, Bugiel E, Dargis R, Fissel A. Introducing crystalline rare -earth oxides into Si technologies. physica status solidi (a). 2008 Apr;205(4):695-707.

39. Zhang FX, Lang M, Wang JW, Becker U, Ewing RC. Structural phase transitions of cubic Gd_2O_3 at high pressures. Physical Review B. 2008 Aug 22;78(6):064114.

40. Kwo J, Hong M, Kortan AR, Queeney KL, Chabal YJ, Opila Jr RL, Muller DA, Chu SN, Sapjeta BJ, Lay TS, Mannaerts JP. Properties of high κ gate dielectrics Gd_2O_3 and Y_2O_3 for Si. Journal of Applied Physics. 2001 Apr 1;89(7):3920-7.

41. Willardson RK, Beer AC. Semiconductors and semimetals. Academic press; 1977 Nov 23.

42. Nolan M, Grigoleit S, Sayle DC, Parker SC, Watson GW. Density functional theory studies of the structure and electronic structure of pure and defective low index surfaces of ceria. Surface Science. 2005 Feb 10;576(1-3):217-29.

43. Schwendt D, Osten HJ, Shekhter P, Eizenberg M. Strain-induced effects on the dielectric constant for thin, crystalline rare earth oxides on silicon. Applied Physics Letters. 2012 Jun 4;100(23):232905.

44. Gribisch P, Fissel A. Tuning of structural and dielectric properties of Gd_2O_3 grown on Si (001). Journal of Applied Physics. 2020 Aug 7;128(5):055108.

45. Roy Chaudhuri A, Fissel A, Osten HJ. Superior dielectric properties for template assisted grown (100) oriented Gd_2O_3 thin films on Si (100). Applied Physics Letters. 2014 Jan 6;104(1):012906.

46. Sitaputra W, Tsu R. Effects of substrate doping on Gd_2O_3 (100)/Si (100) heterostructure. Journal of Vacuum Science & Technology A: Vacuum, Surfaces, and Films. 2013 Mar 21;31(2):021509.

47. Sitaputra W, Tsu R. Defect induced mobility enhancement: Gadolinium oxide (100) on Si (100). Applied Physics Letters. 2012 Nov 26;101(22):222903.

48. Chang WH, Wu SY, Lee CH, Lai TY, Lee YJ, Chang P, Hsu CH, Huang TS, Kwo JR, Hong M. Phase transformation of molecular beam epitaxy-grown nanometer-thick Gd_2O_3 and Y_2O_3 on GaN. ACS applied materials & interfaces. 2013 Feb 27;5(4):1436-41.

49. Fissel A, Czernohorsky M, Osten HJ. Growth and characterization of crystalline gadolinium oxide on silicon carbide for high-K application. Superlattices and Microstructures. 2006 Oct 1;40(4-6):551-6.

50. Chiang TH, Wu SY, Huang TS, Hsu CH, Kwo J, Hong M. Single crystal Gd_2O_3 epitaxially on GaAs (111) A. CrystEngComm. 2014;16(36):8457-62.

51. Moellers M, Margenfeld C, Wietler TF, Osten HJ. Growth of epitaxially stabilized, non-cubic Gd_2O_3 on silicon (111) substrates. Journal of Crystal Growth. 2017 Dec 15;480:141-4.

52. Molle A, Wiemer C, Bhuiyan MN, Tallarida G, Fanciulli M, Pavia G. Cubic-to-monoclinic phase transition during the epitaxial growth of crystalline Gd_2O_3 films on Ge (001) substrates. Applied physics letters. 2007 May 7;90(19):193511.

53. Haque SM, De R, Tripathi S, Mukherjee C, Yadav AK, Bhattacharyya D, Jha SN, Sahoo NK. Effect of oxygen partial pressure in deposition ambient on the properties of RF magnetron sputter deposited Gd_2O_3 thin films. Applied Optics. 2017 Aug 1;56(22):6114-25.

54. Xiang WF, Ni H, Lu HB. In situ RHEED analysis of epitaxial Gd_2O_3 thin films grown on Si (001). Applied Physics A. 2013 Feb;110(2):423-6.

55. Malvino AP, Bates DJ, Hoppe PE. Electronic principles. Glencoe; 1993 Feb.

56. Sze SM, Li Y, Ng KK. Physics of semiconductor devices. John wiley & sons; 2021 Mar 19.

57. Gribisch, P., et al., Influence of nanostructure formation on the crystal structure and morphology of epitaxially grown Gd_2O_3 on Si(001). Acta Crystallographica Section B, 2019. 75(1): p. 59-70.

58. Wu B, Zinkevich M, Aldinger F, Wen D, Chen L. Ab initio study on structure and phase transition of A-and B-type rare-earth sesquioxides Ln_2O_3 (Ln= La –Lu, Y, and Sc) based on density function theory. Journal of Solid State Chemistry. 2007 Nov 1;180(11):3280-7.

59. Momma K, Izumi F. VESTA 3 for three-dimensional visualization of crystal, volumetric and morphology data. Journal of applied crystallography. 2011 Dec 1;44(6):1272-6.

60. Zaumseil P. High-resolution characterization of the forbidden Si 200 and Si 222 reflections. Journal of applied crystallography. 2015 Apr 1;48(2):528-32.

61. Rossmanith E. Approximate calculation of multiple-diffraction patterns based on Renninger's kinematicalsimplest approach'. Journal of applied crystallography. 2000 Jun 1;33(3):921-7.

62. Chang WH, Chang P, Lai TY, Lee YJ, Kwo J, Hsu CH, Hong M. Structural Characteristics of Nanometer Thick Gd_2O_3 Films Grown on GaN (0001). Crystal growth & design. 2010 Dec 1;10(12):5117-22.

63. Chang WH, Wu SY, Lee CH, Lai TY, Lee YJ, Chang P, Hsu CH, Huang TS, Kwo JR, Hong M. Phase transformation of molecular beam epitaxy-grown nanometer-thick Gd_2O_3 and Y_2O_3 on GaN. ACS applied materials & interfaces. 2013 Feb 27;5(4):1436-41..

64. Mishra M, Kuppusami P, Ramya S, Ganesan V, Singh A, Thirumurugesan R, Mohandas E. Microstructure and optical properties of Gd_2O_3 thin films prepared by pulsed laser deposition. Surface and Coatings Technology. 2015 Jan 25;262:56-63.

65. Lopez-Lazcano CA, Mart ínez-Falomir GG, Almaral-Sánchez JL. Deposition of ZnO and Gd_2O_3 by co-sputtering to enable ZnO- Gd_2O_3 based PIN junction diodes. Materials Science in Semiconductor Processing. 2020 Jun 1;111:105005.

66. Yilmaz E, Tu ğay E, Aktağ A, Yildiz I, Parlak M, Turan R. Surface morphology and depth profile study of $Cd_{1-x}Zn_xTe$ alloy nanostructures. Journal of alloys and compounds. 2012 Dec 25;545:90-8.

67. Ferrara MC, Altamura D, Schioppa M, Tapfer L, Nichelatti E, Pilloni L, Montecchi M. Growth, characterization and optical properties of nanocrystalline gadolinia thin films prepared by sol – gel dip coating. Journal of Physics D: Applied Physics. 2008 Oct 30;41(22):225408.

68. Houssa M, Tuominen M, Naili M, Afanas'ev V, Stesmans A, Haukka S, Heyns MM. Trap-assisted tunneling in high permittivity gate dielectric stacks. Journal of Applied Physics. 2000 Jun 15;87(12):8615-20.

69. Blank O, Reisinger H, Stengl R, Gutsche M, Wiest F, Capodieci V, Schulze J, Eisele I. A model for multistep trap-assisted tunneling in thin high-k dielectrics. Journal of applied physics. 2005 Feb 15;97(4):044107.

70. Lipp E, Shahar Z, Bittel BC, Lenahan PM, Schwendt D, Osten HJ, Eizenberg M. Trap-assisted conduction in Pt-gated Gd_2O_3/Si capacitors. Journal of Applied Physics. 2011 Apr 1;109(7):073724.

71. Laha A, Bugiel E, Wang JX, Sun QQ, Fissel A, Osten HJ. Effect of domain boundaries on the electrical properties of crystalline Gd_2O_3 thin films. Applied Physics Letters. 2008 Nov 3;93(18):182907.

72. Czernohorsky M, Bugiel E, Osten HJ, Fissel A, Kirfel O. Impact of oxygen supply during growth on the electrical properties of crystalline Gd_2O_3 thin films on Si (001). Applied Physics Letters. 2006 Apr 10;88(15):152905.

73. Kaya S, Lok R, Aktag A, Seidel J, Yilmaz E. Frequency dependent electrical characteristics of $BiFeO_3$ MOS capacitors. Journal of alloys and compounds. 2014 Jan 15;583:476-80.

74. Fehan SK, Naeem GA, Jabur YK. Studying the influence of fast neutrons & gamma-ray on the electrical characteristics of pn. Journal of university of Anbar for Pure science. 2007;1(2).

75. Akta ğ A, Mutale A, Yılmaz E. Determination of frequency and voltage dependence of electrical properties of Al/(Er_2O_3/SiO_2/n-Si)/Al MOS capacitor. Journal of Materials Science: Materials in Electronics. 2020 Jun;31(11):9044-51.

76. Kahraman A, Deevi SC, Yilmaz E. Influence of frequency and gamma irradiation on the electrical characteristics of Er_2O_3, Gd_2O_3, Yb_2O_3, and HfO_2 MOS-based devices. Journal of Materials Science. 2020 Jul;55(19):7999-8040.

7. APPENDICES

Appendix 1

Gd_2O_3 sample specifications

Ganzhou Wanfeng Adv. Materials Tech. Co., Ltd.

Business Type	Trading Company	Country/ Region	Jiangxi, China
Main Products	Rare Earth Oxides, Rare Earth Metals&Alloys, Rare Earth Salts, RE Polishing Powder, RE Functional Materials	Year Established	2011

Place of Origin:	Jiangxi, China
Brand Name:	WANFENG
Model Number:	REO-Gd
Composition:	Gadolinium
Product Type:	Rare Earth Oxide
Content(percent):	99.9% Min
Application:	Industry
Grade:	Gadolinium Oxide
Appearance:	White Powder
Formula:	Gd_2O_3
type:	Rare Earth Oxide Podwer
Style:	Gadolinium oxide
application:	Optical glasses,bubble domain and electronic industry

Purity:	99.9% min
Solubility:	Water insoluble, but soluble in the acids.
CAS No.:	12064-62-9
EC No.:	235-060-9
Storage:	Keep sealed and store in dry and cool places

Gadolinium Oxide Gd2O3

Purity		3N	3N5	4N	4N5	5N	5N5
TREO % min.		99	99	99	99	99	99
Gd_2O_3 /TREO % min.		99.9	99.95	99.99	99.995	99.999	99.9995
Rare earth impurities % max.	La_2O_3	Total 0.1 (Sm2O3+ Eu2O3+ Tb4O7+ Dy2O3+ Y2O3)	Total 0.05 (Sm2O3+ Eu2O3+ Tb4O7+ Dy2O3+ Y2O3)	Total 0.0040	0.0002	0.0001	0.0001
	CeO_2				0.0002	0.00005	0.00005
	Pr_6O_{11}				0.0002	0.00005	0.00005
	Nd_2O_3				0.0005	0.0001	0.0001
	Ho_2O_3				0.0005	0.00005	0.00005
	Er_2O_3				0.0002	0.00005	0.00005
	Tm_2O_3				0.0002	0.00005	0.00005
	Yb_2O_3				0.0002	0.00005	0.00005
	Lu_2O_3				0.0002	0.00005	0.00005
	Sm_2O_3			0.001	0.0005	0.00005	0.00005
	Eu_2O_3			0.0015	0.0005	0.0001	0.0001
	Tb_4O_7			0.0015	0.0005	0.0001	0.0001
	Dy_2O_3			0.001	0.0005	0.0001	0.0001
	Y_2O_3			0.001	0.0005	0.0001	0.0001
Non rare earth impurities % max.	Fe_2O_3	0.003	0.001	0.0005	0.0003	0.0002	0.0001
	SiO_2	0.006	0.005	0.005	0.003	0.002	0.001
	CaO	0.005	0.003	0.002	0.001	0.0005	0.0005
	CuO	—	0.001	0.0005	0.0003	0.0002	0.0001
	PbO	—	0.001	0.001	0.0005	0.0003	0.0002
	NiO	—	0.001	0.001	0.0005	0.0003	0.0001
	Al_2O_3	0.04	0.03	0.01	0.01	0.005	0.001
	Cl^-	0.05	0.03	0.02	0.015	0.01	0.01
L.O.I and Water % Max.		1	1	1	1	1	1

Remark: All the experiment is without water.

Appendix 2

Specification of P-type (CZ) Silicon wafers